Winters KA, Jiang Z, Xu W, Li S, Ammous Z, Jayakar P, Wierenga KJ (2012) Re-assigned diagnosis of D4ST1-deficient Ehlers-Danlos syndrome (adducted thumb-clubfoot syndrome) after initial diagnosis of Marden-Walker syndrome. Am J Med Genet A 158A:2935–2940

Yasui H, Adachi Y, Minami T, Ishida T, Kato Y, Imai K (2003) Combination therapy of DDAVP and conjugated estrogens for a recurrent large subcutaneous hematoma in Ehlers–Danlos syndrome. Am J Hematol 72:71–72

Zhang L, Müller T, Baenziger JU, Janecke AR (2010) Congenital disorders of glycosylation with emphasis on loss of dermatan-4-sulfotransferase. Prog Mol Biol Transl Sci 93:289–307

International Journal of Cardiology 173 (2014) e63–e66

Contents lists available at ScienceDirect

International Journal of Cardiology

journal homepage: www.elsevier.com/locate/ijcard

Letter to the Editor

Bilateral giant coronary aneurysms in a 40-year-old male with Noonan syndrome caused by a *KRAS* germline mutation

Naoki Fujimoto [a,*], Hiroshi Nakajima [b], Emiyo Sugiura [b], Kaoru Dohi [b], Shinji Kanemitsu [c], Norikazu Yamada [b], Yoko Aoki [d], Kaname Nakatani [a], Hideto Shimpo [c], Tsutomu Nobori [a], Masaaki Ito [b]

[a] Department of Molecular and Laboratory Medicine, Mie University Graduate School of Medicine, Tsu, Japan
[b] Department of Cardiology and Nephrology, Mie University Graduate School of Medicine, Tsu, Japan
[c] Department of Thoracic and Cardiovascular Surgery, Mie University Graduate School of Medicine, Tsu, Japan
[d] Department of Medical Genetics, Tohoku University School of Medicine, Sendai, Japan

ARTICLE INFO

Article history:
Received 7 February 2014
Accepted 15 March 2014
Available online 21 March 2014

Keywords:
Noonan syndrome
Coronary aneurysm
KRAS germline mutation

We report a case of a 40-year-old man who was admitted to our hospital for the evaluation and treatment of chest discomfort on exertion. He had previously been followed for post-natal growth deficiency, strabismus, mental retardation, epilepsy, and moderate mitral regurgitation. On admission, he was 142 cm in height and 42 kg in weight. Physical examination revealed orbital hypertelorism, ptosis, a webbed neck, and low-set ears with no jugular vein dilatation or peripheral edema. Cardiac auscultation showed a 3/6 late systolic murmur and S4. ECG showed normal sinus rhythm, poor R wave progression in the precordial leads, and an incomplete right bundle brunch block. Chest X-ray showed pulmonary congestion and marked cardiomegaly, with a cardio-thoracic ratio of 71%.

Echocardiography revealed severe mitral regurgitation due to prolapse of the anterior and posterior mitral leaflets (Fig. 1A–C) and aneurysms near the left coronary artery (LCA) (Fig. 1D), and the right coronary artery (RCA). No left ventricular hypertrophy, wall motion abnormality, or atrial septal defects were observed. A CT scan also revealed coronary aneurysms with no pulmonic stenosis; one aneurysm near the LCA measured 40 × 32 mm, and the other near the RCA 13 × 12 mm (Fig. 2A–B). Total occlusion of right common iliac artery with subsequent aneurysmal change, and dilatation of left common iliac artery were observed. Coronary angiography was then performed to elucidate the complex anatomy of the aneurysms and coronary arteries (Fig. 2C–D). A giant aneurysm containing a thrombus originated from the proximal LCA (Fig. 3 A–B). The left anterior descending artery was occluded with small collaterals from the left circumferential artery (LCX). The other aneurysm originated from the proximal RCA (Fig. 3 C–D), and the distal portion of the RCA was occluded with collaterals from the LCX.

It was thought that severe mitral regurgitation from a prolapsed leaflet and myocardial ischemia due to coronary aneurysms and severe occlusive coronary artery disease were responsible for his symptoms. The patient underwent a surgical procedure that involved mitral valve repair, ligation of the aneurysms, and coronary artery bypass grafting. The post-operative course was complicated by ventricular fibrillation during the operation and the patient unfortunately expired due to refractory congestive heart failure 13 days after surgery.

Genetic screening confirmed a heterozygous nucleotide change within exon 4b of the *KRAS* gene (c.458A>T), causing the amino acid substitution D153V, whose clinical phenotype was Noonan/Cardio-facio-cutaneous (CFC) syndrome [1,2].

Noonan syndrome was first described in 1963, and CFC syndrome was described in 1986. These syndromes have many overlapping manifestations such as short stature, characteristic facial appearance, mental retardation and heart abnormalities, including pulmonic stenosis, hypertrophic cardiomyopathy, and atrial septal defects. While, coronary aneurysms with occlusive coronary artery disease, as seen in our case, have been rarely reported in an adult patient with these syndromes [3]. Moreover, it was unclear when and how these cardiovascular changes had occurred during his life. We conclude that patients with Noonan/CFC syndrome may have the risks for coronary aneurysms and severe cardiovascular disease. Thus, careful cardiovascular follow-up should be performed in their entire life.

References

[1] Schubbert S, Zenker M, Rowe SL, et al. Germline KRAS mutations cause Noonan syndrome. Nat Genet 2006;38:331–6.
[2] Niihori T, Aoki Y, Narumi Y, et al. Germline KRAS and BRAF mutations in cardio-facio-cutaneous syndrome. Nat Genet 2006;38:294–6.
[3] Loukas M, Dabrowski M, Kantoch M, Ruzyłło W, Waltenberger J, Giannikopoulos P. A case report of Noonan's syndrome with pulmonary valvar stenosis and coronary aneurysms. Med Sci Monit 2004;10:CS80–3.

* Corresponding author at: Department of Molecular and Laboratory Medicine, Mie University Graduate School of Medicine, 2-174 Edobashi, Tsu 514-8507, Japan. Tel.: +81 59 231 5161; fax: +81 59 231 5250.
E-mail address: naokifujimo@clin.medic.mie-u.ac.jp (N. Fujimoto).

http://dx.doi.org/10.1016/j.ijcard.2014.03.135

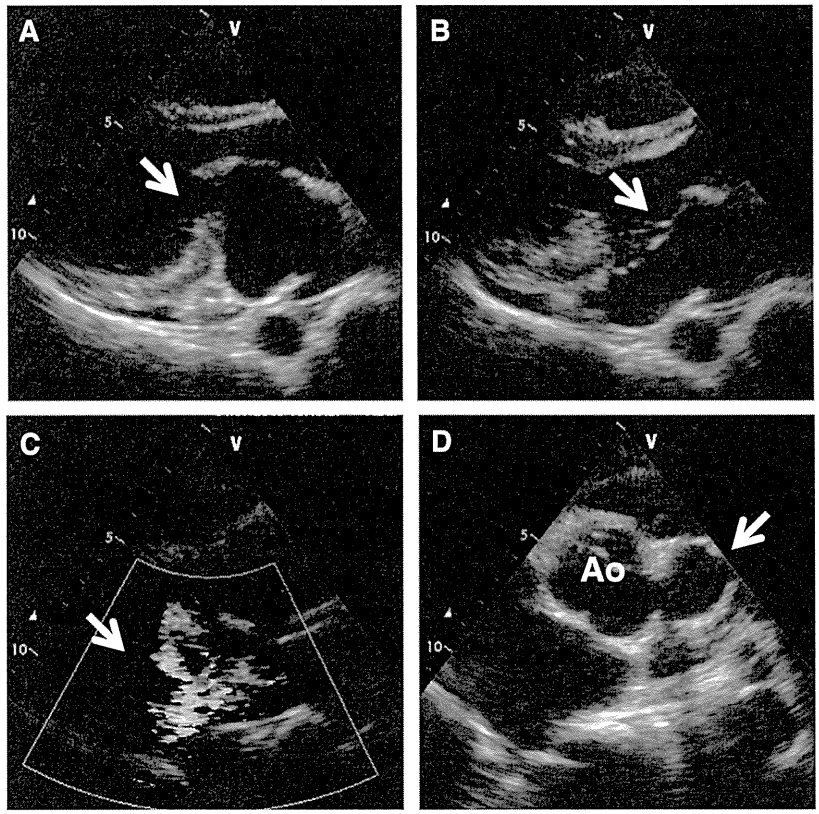

Fig. 1. Two-dimensional echocardiogram at end-diastole (A) and end-systole (B–C) showing severe mitral regurgitation due to mitral prolapse (arrow). Short axis image at the level of aortic valve with a giant aneurysm near left coronary artery (D).

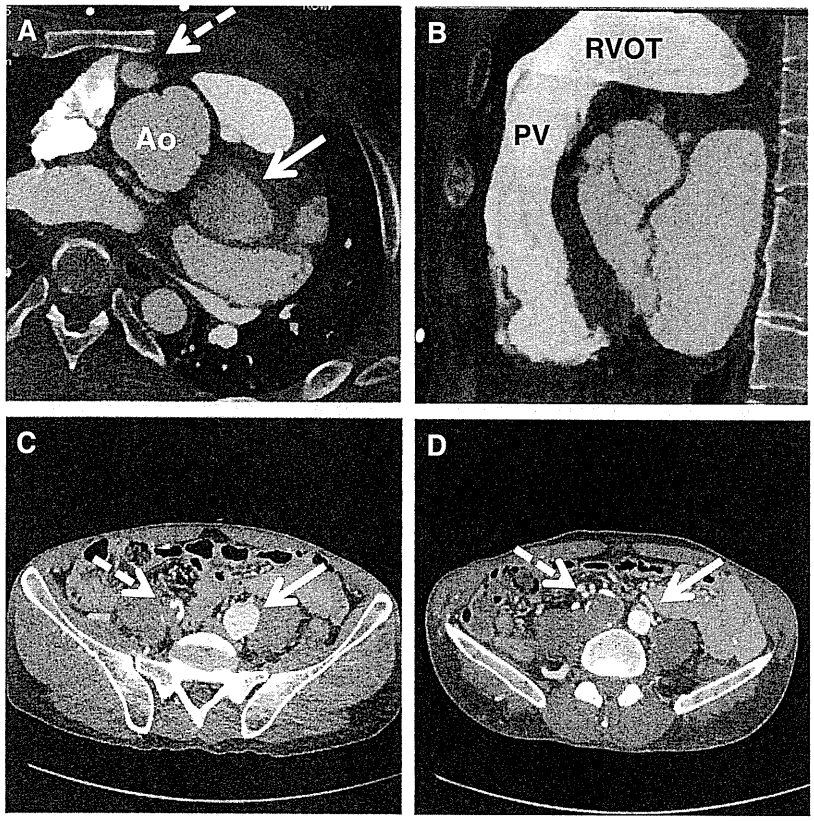

Fig. 2. Computed tomography (CT) axial view showing aneurysms near left coronary artery (arrow) and the right coronary artery (broken arrow)(A). CT sagittal view with intact pulmonic valve (PV) and right ventricular outflow tract (RVOT). CT axial view at proximal (C) and distal (D) levels of common iliac artery showing occluded right common iliac artery (broken arrow) and dilated left common iliac artery (arrow).

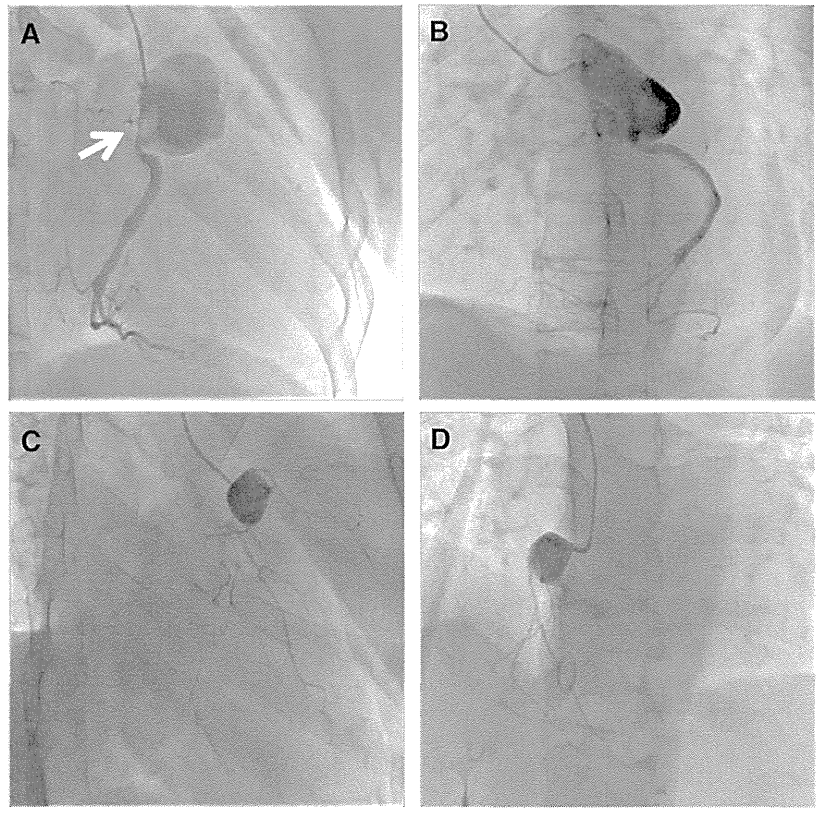

Fig. 3. Left coronary artery angiography in right anterior oblique (RAO; panel A) and left anterior oblique (LAO) views (panel B) showing a giant left coronary aneurysm containing a thrombus near the origin of the left circumflex coronary artery (arrow). Right coronary artery angiography in RAO caudal (C) and LAO cranial (D) views showing a right coronary aneurysm and coronary artery stenosis.

Human Molecular Genetics, 2014, Vol. 23, No. 16 **4315–4327**
doi:10.1093/hmg/ddu148
Advance Access published on April 4, 2014

Activating mutations in *RRAS* underlie a phenotype within the RASopathy spectrum and contribute to leukaemogenesis

Elisabetta Flex[1,†], Mamta Jaiswal[3,†], Francesca Pantaleoni[1,‡], Simone Martinelli[1,‡], Marion Strullu[4,7,‡], Eyad K. Fansa[3,‡], Aurélie Caye[4,7], Alessandro De Luca[8], Francesca Lepri[9], Radovan Dvorsky[3], Luca Pannone[1], Stefano Paolacci[1], Si-Cai Zhang[3], Valentina Fodale[1], Gianfranco Bocchinfuso[10], Cesare Rossi[11], Emma M.M. Burkitt-Wright[12], Andrea Farrotti[10], Emilia Stellacci[1], Serena Cecchetti[2], Rosangela Ferese[8], Lisabianca Bottero[1], Silvana Castro[13], Odile Fenneteau[5], Benoît Brethon[6], Massimo Sanchez[2], Amy E. Roberts[14], Helger G. Yntema[15], Ineke Van Der Burgt[15], Paola Cianci[16], Marie-Louise Bondeson[17], Maria Cristina Digilio[9], Giuseppe Zampino[18], Bronwyn Kerr[12], Yoko Aoki[19], Mignon L. Loh[20], Antonio Palleschi[10], Elia Di Schiavi[13,¶], Alessandra Carè[1], Angelo Selicorni[16], Bruno Dallapiccola[9], Ion C. Cirstea[3,21], Lorenzo Stella[10], Martin Zenker[22], Bruce D. Gelb[23,24,25], Hélène Cavé[4,7,§], Mohammad R. Ahmadian[3,§] and Marco Tartaglia[1,§,*]

[1]Dipartimento di Ematologia, Oncologia e Medicina Molecolare and [2]Dipartimento di Biologia Cellulare e Neuroscienze, Istituto Superiore di Sanità, Rome 00161, Italy, [3]Institut für Biochemie und Molekularbiologie II, Medizinische Fakultät der Heinrich-Heine Universitat, Düsseldorf 40225, Germany, [4]Genetics Department, [5]Biological Hematology Department and [6]Pediatric Hematology Department, Robert Debré Hospital, Paris 75019, France, [7]INSERM UMR_S940, Institut Universitaire D'Hématologie (IUH), Université Paris-Diderot Sorbonne-Paris-Cité, Paris 75010, France, [8]Laboratorio Mendel, Istituto di Ricovero e Cura a Carattere Scientifico-Casa Sollievo Della Sofferenza, Rome 00198, Italy, [9]Ospedale Pediatrico 'Bambino Gesù', Rome 00165, Italy, [10]Dipartimento di Scienze e Tecnologie Chimiche, Università 'Tor Vergata', Rome 00133, Italy, [11]UO Genetica Medica, Policlinico S.Orsola-Malpighi, Bologna 40138, Italy, [12]Genetic Medicine, Academic Health Science Centre, Central Manchester University Hospitals NHS Foundation Trust, Manchester M13 9WL, UK, [13]Istituto di Genetica e Biofisica 'A. Buzzati Traverso', Consiglio Nazionale Delle Ricerche, Naples 80131, Italy, [14]Department of Cardiology and Division of Genetics, and Department of Medicine, Boston Children's Hospital, Boston, MA 02115, USA, [15]Department of Human Genetics, Radboud University Medical Centre, and Nijmegen Centre for Molecular Life Sciences, Radboud University, Nijmegen 6500, The Netherlands, [16]Genetica Clinica Pediatrica, Clinica Pediatrica Università Milano Bicocca, Fondazione MBBM, A.O. S. Gerardo, Monza 20900, Italy, [17]Department of Immunology, Genetics and Pathology, Uppsala University, Uppsala 75237, Sweden, [18]Istituto di Clinica Pediatrica, Università Cattolica del Sacro Cuore, Rome 00168, Italy, [19]Department of Medical Genetics, Tohoku University School of Medicine, Sendai 980-8574, Japan, [20]Department of Pediatrics, Benioff Children's Hospital, University of California School of Medicine, and the Helen Diller Family Comprehensive Cancer Center, San Francisco, CA 94143, USA, [21]Leibniz Institute for Age Research, Jena 07745, Germany, [22]Institute of Human Genetics, University Hospital of

*To whom correspondence should be addressed at: Dipartimento di Ematologia, Oncologia e Medicina Molecolare, Istituto Superiore di Sanità, Viale Regina Elena, 299, 00161 Rome, Italy. Tel: +39 0649902569; Fax: +39 0649902850; Email: marco.tartaglia@iss.it
†These authors contributed equally to this project.
‡These authors contributed equally to this project.
¶Present address: Institute of Bioscience and BioResources, Consiglio Nazionale delle Ricerche, Naples 80131, Italy.
§These authors contributed equally as the senior investigators for this project.

Magdeburg, Otto-von-Guericke-University, Magdeburg 39120, Germany, [23]Department of Pediatrics and [24]Department of Genetics and [25]Department of Genomic Sciences, Mindich Child Health and Development Institute, Icahn School of Medicine at Mount Sinai, New York, NY 10029, USA

Received December 10, 2013; Revised and Accepted March 4, 2014

RASopathies, a family of disorders characterized by cardiac defects, defective growth, facial dysmorphism, variable cognitive deficits and predisposition to certain malignancies, are caused by constitutional dysregulation of RAS signalling predominantly through the RAF/MEK/ERK (MAPK) cascade. We report on two germline mutations (p.Gly39dup and p.Val55Met) in *RRAS*, a gene encoding a small monomeric GTPase controlling cell adhesion, spreading and migration, underlying a rare (2 subjects among 504 individuals analysed) and variable phenotype with features partially overlapping Noonan syndrome, the most common RASopathy. We also identified somatic *RRAS* mutations (p.Gly39dup and p.Gln87Leu) in 2 of 110 cases of non-syndromic juvenile myelomonocytic leukaemia, a childhood myeloproliferative/myelodysplastic disease caused by upregulated RAS signalling, defining an atypical form of this haematological disorder rapidly progressing to acute myeloid leukaemia. Two of the three identified mutations affected known oncogenic hotspots of *RAS* genes and conferred variably enhanced RRAS function and stimulus-dependent MAPK activation. Expression of an RRAS mutant homolog in *Caenorhabditis elegans* enhanced RAS signalling and engendered protruding vulva, a phenotype previously linked to the RASopathy-causing SHOC2^{S2G} mutant. Overall, these findings provide evidence of a functional link between RRAS and MAPK signalling and reveal an unpredicted role of enhanced RRAS function in human disease.

INTRODUCTION

Signalling elicited by activated cell surface receptors and transduced through RAS proteins to the RAF/MEK/ERK and PI3K/AKT cascades is central to cell proliferation, survival, differentiation and metabolism (1,2). Owing to this nodal role, enhanced traffic through RAS proteins and their downstream effectors has been established to have a major impact on oncogenesis (3,4). This signalling network also controls early and late developmental processes (e.g. organogenesis, morphology determination, synaptic plasticity and growth), and germline mutations in a number of genes encoding transducers and modulatory proteins participating in the RAS/MAPK signalling pathway have been causally linked to Noonan syndrome (NS) (5), one of the most common diseases affecting development and growth, and a group of clinically related syndromes, the so-called RASopathies (6–8). In this family of disorders, constitutional dysregulation of RAS signalling can be caused by enhanced activation of HRAS, KRAS and NRAS (RAS proteins hereafter), aberrant function of upstream signal transducers or effectors (PTPN11/SHP2, SOS1, SHOC2, RAF1, BRAF, MAP2K1/MEK1 and MAP2K2/MEK2) or inefficient down modulation by feedback mechanisms (CBL, NF1 and SPRED1). More recently, *RIT1*, encoding a monomeric GTPase structurally linked to RAS proteins, was identified as disease gene implicated in NS (9), extending the concept of 'RASopathy gene' to a transducer that contributes to signal propagation through RAS effector pathways but does not belong to the RAS/MAPK signalling backbone.

Clinical manifestations of RASopathies include postnatal reduced growth, a wide spectrum of cardiac defects, facial dysmorphism, ectodermal and skeletal anomalies and variable cognitive deficits (5,8,10). Consistent with the key role of most RASopathy genes in oncogenesis, these disorders are also characterized by variably increased risk for certain haematologic malignancies and other paediatric cancers (6,7,11,12). Most of these conditions are genetically heterogeneous, and the underlying disease gene has not been identified yet for a still significant fraction of cases. Based on the strict mechanistic link between the molecular events controlling development and contributing to oncogenesis, these 'missing' genes represent excellent candidate oncogenes/tumour suppressors.

Here, we report that constitutional dysregulation of RRAS function is associated with a Mendelian trait within the RASopathy spectrum and that somatically acquired mutations in the same gene occur in an aggressive form of juvenile myelomonocytic leukaemia (JMML), a rare childhood myeloproliferative/myelodysplastic neoplasm representing the archetypal somatic RASopathy (13), rapidly progressing to acute myeloid leukaemia (AML). We also demonstrate that RASopathy-causing *RRAS* mutations are activating and promote signalling perturbation by enhancing stimulus-dependent MEK, ERK and, at a lower extent, AKT phosphorylation.

RESULTS

Identification of candidate disease genes and *RRAS* mutation analysis

While the core of the machinery implicated in RAS signalling has been characterized comprehensively, signal propagation through this network is likely to include a larger number of proteins playing a modulatory or structural role (14), whose aberrant or defective function is expected to perturb development and

contribute to oncogenesis. Based on this assumption, we used a protein interaction/functional association network analysis to select a panel of genes encoding proteins functionally linked to the RAS signalling network as candidates for NS or a related RASopathy (15). Candidate gene selection was based on the use of the previously identified RASopathy genes as 'seed' proteins (i.e. proteins used to build the interaction/functional networks), and considering a panel of databases to construct functional subnetworks (Supplementary material, Table S1 and Fig. S1). Sequence scanning of the best candidates in a RASopathy cohort including 96 unrelated subjects negative for mutations in known disease genes allowed the identification of a functionally relevant *RRAS* change (c.163G>A, p.Val55Met) (Supplementary material, Fig. S2) in an adult subject with clinical features suggestive of NS but lacking sufficient characteristics to allow a definitive diagnosis (Supplementary material, Table S2). Parental DNA was not available for segregation analysis. The mutation was not identified among >400 population-matched unaffected individuals, indicating that it did not represent a common polymorphic nucleotide substitution. This change, rs368625677 (dbSNP 138), had been described in 1/13,006 alleles in the NHLBI Exome Sequencing Project (http://eversusgs.washington.edu/EVS/). Of note, similar frequencies have been reported in the same database for recurrent RASopathy-causing mutations (e.g. c.922A>G in *PTPN11*, and c.1259G>A in *CBL*). Mutation analysis was extended to additional 408 patients with NS or a clinically related phenotype tested negative for mutations in the major NS disease genes (see Materials and Methods), allowing to identify one sporadic case heterozygous for a three-nucleotide duplication (c.116_118dup, p.Gly39dup) (Supplementary material, Fig. S2). Parental DNA sequencing of the relevant exon demonstrated the *de novo* origin of the variant, and STR genotyping confirmed paternity. In this subject, the duplication was documented in DNA obtained from skin fibroblasts, excluding a somatic event restricted to haematopoietic cells. The subject had features reminiscent of NS (Fig. 1A and Supplementary material, Table S2), with onset of AML suspected to represent a blast crisis of JMML (Supplementary material, Table S3 and Fig. S3). In this patient, exome sequencing performed on leukaemic and non-leukaemic DNA failed to disclose any additional relevant germline/somatic change affecting genes known to be mutated in RASopathies and JMML, as well as genes directly linked to the RAS signalling network, further supporting the causal role of the identified *RRAS* lesion. Based on this association, the occurrence of *RRAS* mutations was also explored in a panel of genomic DNAs obtained from bone marrow aspirates/circulating leukocytes of 110 subjects with JMML. Heterozygosity for the previously identified Gly^{39} duplication and the c.260A>T (p.Gln87Leu) change was observed in two patients with JMML rapidly progressing to AML (Supplementary material, Table S3 and Fig. S3). Both lesions were absent in non-leukaemic DNA, indicating their somatic origin (Supplementary material, Fig. S2). These subjects also carried a somatic *NRAS* mutation, suggesting that the two hits might cooperate with this particularly severe form of disease. Sequencing of isolated JMML myeloid colonies in patient 14385 showed that *NRAS* and *RRAS* mutations coexisted in the same progenitors but failed to establish their sequence of appearance during leukaemogenesis, not allowing to discriminate whether the latter was involved in initiation or progression of disease.

Structural analyses

RRAS encodes a 23-kD a membrane-bound monomeric GTPase with 55–60% amino acid identity to RAS proteins (16). This highly conserved structure is flanked by a unique 26-amino acid region at the *N*-terminus (Fig. 1B). Similarly to the other RAS family proteins, RRAS binds to GTP and GDP with high affinity and specificity and functions as a molecular switch by cycling between active, GTP-bound and inactive, GDP-bound states (17). RRAS is activated by guanine nucleotide exchange factors (GEFs) in response to signals elicited by cell surface receptors. In the GTP-bound state, two functionally conserved regions, switch I and switch II (Fig. 1B), undergo a conformational change enabling RRAS to bind to and activate effector proteins. This interaction is terminated by hydrolysis of GTP to GDP, which is promoted by GTPase-activating proteins (GAPs) and results in switching towards the inactive conformation. Disease-associated *RRAS* mutations affected residues highly conserved among orthologs and paralogs (Supplementary material, Fig. S4) residing in the GTP-binding pocket (Fig. 1C) and were predicted to be damaging with high confidence (Supplementary material, Table S4). Among them, Gln^{87}, homolog of Gln^{61} in RAS proteins, is directly involved in catalysis (18,19). The p.Gln87Leu substitution had previously been reported as a rare somatic event in lung carcinoma, and mutations affecting Gln^{61} are among the most recurrent oncogenic lesions in *RAS* genes (COSMIC database, http://cancer.sanger.ac.uk/cancergenome/projects/cosmic/). Likewise, p.Gly39dup altered the G1 motif participating in GTP/GDP binding and GTPase activity (Fig. 1B). Within this motif, Gly^{12} and Gly^{13} (Gly^{38} and Gly^{39} in RRAS) represent major mutation hot-spots in human cancer (COSMIC database) and account for the majority of germline *HRAS* mutations causing Costello syndrome (20). Of note, analogous insertions in RAS proteins have been reported in JMML and other malignancies (21–24). In contrast, no somatic/germline *RAS* mutation affecting Val^{29}, homolog of Val^{55} in RRAS, had previously been reported. Val^{55} side-chain is not directly involved in GTP/GDP binding, GTP hydrolysis or interaction with effectors. However, it has been reported that H-bonds are possible between the backbone of Val^{29} in HRAS and GDP/GTP (25). Furthermore, it has been suggested that Val^{29} can play a role in the transition between the GDP- and GTP-bound states (26), as supported by the evidence that the Val29Gly substitution in HRAS accelerates the GDP/GTP exchange *in vitro* (27).

Molecular dynamics (MD) simulations were performed to predict *in silico* the effects of p.Val55Met on the structure and dynamics of RRAS (Fig. 2). The mutation was introduced in the available crystallographic structure of RRAS in complex with GDP and Mg^{2+}, and the system was simulated in water for 200 ns. For comparison, MD simulations were also performed using the wild-type protein, which maintained a stable structure along the whole simulation, as expected (Fig. 2A, left panel). In contrast, a dramatic local structural transition extending up to the switch I region (residues 58–64), which mediates effector binding, was documented for the $RRAS^{V55M}$ mutant, after ~80 ns (Fig. 2A, right panel). This conformational transition resulted in an increased solvent exposure of Met^{55}, in agreement with the higher hydrophilicity of this residue compared with Val, and was accompanied by the formation of a stable

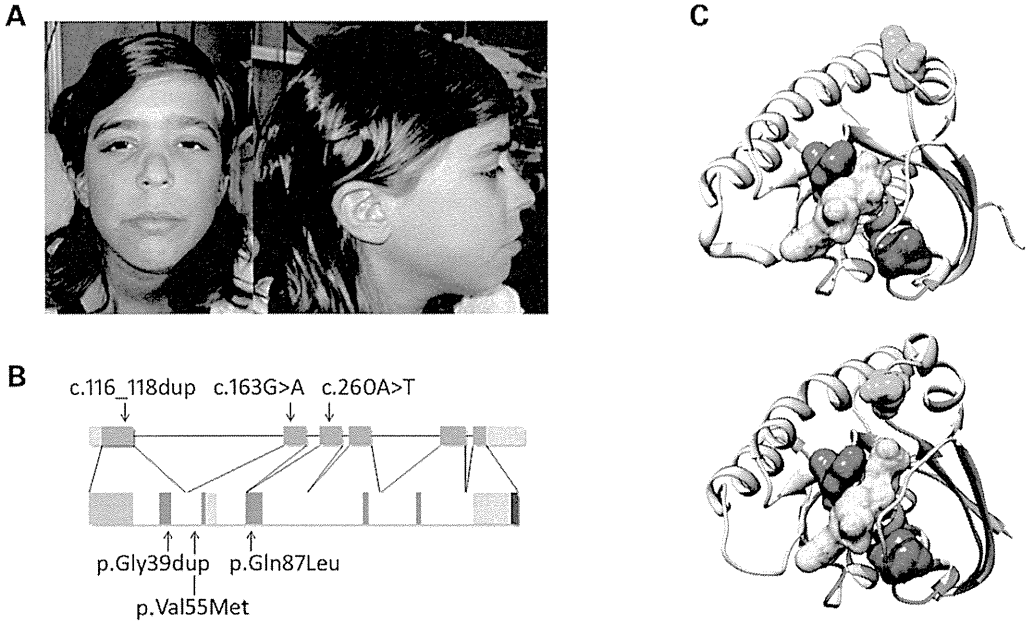

Figure 1. RASopathy-causing and leukaemia-associated *RRAS* mutations. (**A**) Facial features of the affected subject (9802) heterozygous for the *de novo* germline c.116_118dup. (**B**) *RRAS* exon–intron arrangement with coding exons as blue boxes. RRAS functional motifs include the GTP/GDP binding domain (G1 to G5, starting from the *N*-terminus) (red), switch I (light green), switch II (dark green) and hypervariable region (light brown) with the *C*-terminal CAAX motif (dark brown). The unique *N*-terminal region is also shown (violet). Location of disease-associated mutations is reported. (**C**) Position of affected residues on the three-dimensional structure of RRAS in its GDP-bound, inactive state (PDB: 2FN4) (above) and that of non-hydrolysable GTP analogue (GppNHp)-bound, active HRAS (PDB: 5P21) (below). The red surface indicates Gly^{39} and Val^{40} (Gly^{13} and Val^{14}, in HRAS), whereas Val^{55} (Val^{29}) and Gln^{87} (Gln^{61}) are shown in blue and green, respectively. GDP is reported as semi-transparent yellow surface.

cluster involving residues Ile^{50}, Met^{55} and Tyr^{58} (Fig. 2A and Supplementary material, Table S5) permitted by the unbranched and long side-chain of Met^{55}. No further significant conformational changes were observed for the remaining interval of the simulation. The major effect of this structural rearrangement was to increase exposure of GDP to the solvent (Fig. 2B), with an almost doubled solvent accessible surface area of the nucleotide after the conformational transition. This structural rearrangement was accompanied by a perturbation of the intermolecular H-bond network stabilizing GDP binding, with loss of the H-bonds between residues at codons 55 and 56, and GDP (Supplementary material, Table S5). Of note, a possible impact of the described structural transition on RRAS binding to GEF proteins, which bind to this region and mediate GDP release, was also noticed. Specifically, we observed that after the conformational rearrangement, the $RRAS^{V55M}$ region implicated in GEF binding populated a structure similar to that assumed in RAS/GEF complexes (Fig. 2C), suggesting a possible enhanced interaction of the disease-associated RRAS mutant with GEFs. In particular, Tyr^{58} was observed to adopt a side-chain orientation very similar to that of the RAS homolog Tyr^{32} in the HRAS/SOS1 complex, which has been shown to contribute to the structural rearrangements of switch I and interaction with GEFs (28–30).

Overall, these data supported an activating role of p.Val55Met through enhanced GDP release as a result of a decreased affinity for the nucleotide and/or enhanced interaction with a GEF.

Biochemical and functional characterization of RRAS mutants

Previous studies documented the gain-of-function role of p.Gln87Leu on RRAS function, and MAPK and PI3K/AKT signalling (31). To characterize the impact of p.Val55Met and p.Gly39dup on protein function, we analysed the intrinsic and GEF-accelerated nucleotide exchange reaction of these mutants. Dissociation kinetics analysis demonstrated a dramatically increased intrinsic ($RRAS^{G39dup}$) and GEF-stimulated ($RRAS^{G39dup}$ and $RRAS^{V55M}$) dissociation rate of mantGDP, indicating a facilitated nucleotide release in both mutants (Fig. 3A). RAS proteins exhibit low intrinsic GTPase activity that is enhanced by GAPs (32). Assessment of $RRAS^{G39dup}$ and $RRAS^{V55M}$ GTPase activity documented a significantly reduced intrinsic and GAP-stimulated GTP hydrolysis in the former (Fig. 3B and Supplementary material, Fig. S5). Finally, the interaction of RRAS proteins with various effectors was analysed by fluorescence polarization (Fig. 3C). While $RRAS^{WT}$ was found to bind to RAF1, RALGDS, RASSF5 and PLCE1 less efficiently than HRAS, an increased binding affinity to PIK3CA was observed. Compared with $RRAS^{WT}$, aberrant binding behaviour of the two RRAS mutants was demonstrated, with $RRAS^{G39dup}$ exhibiting an increased binding affinity towards PIK3CA, RAF1, PLCE1 and RASSF5, and $RRAS^{V55M}$ to RALGDS.

To gain further insights into the impact of disease-causing mutations on RRAS functional dysregulation and explore their effects on RAS signalling, the activation state of RRAS proteins

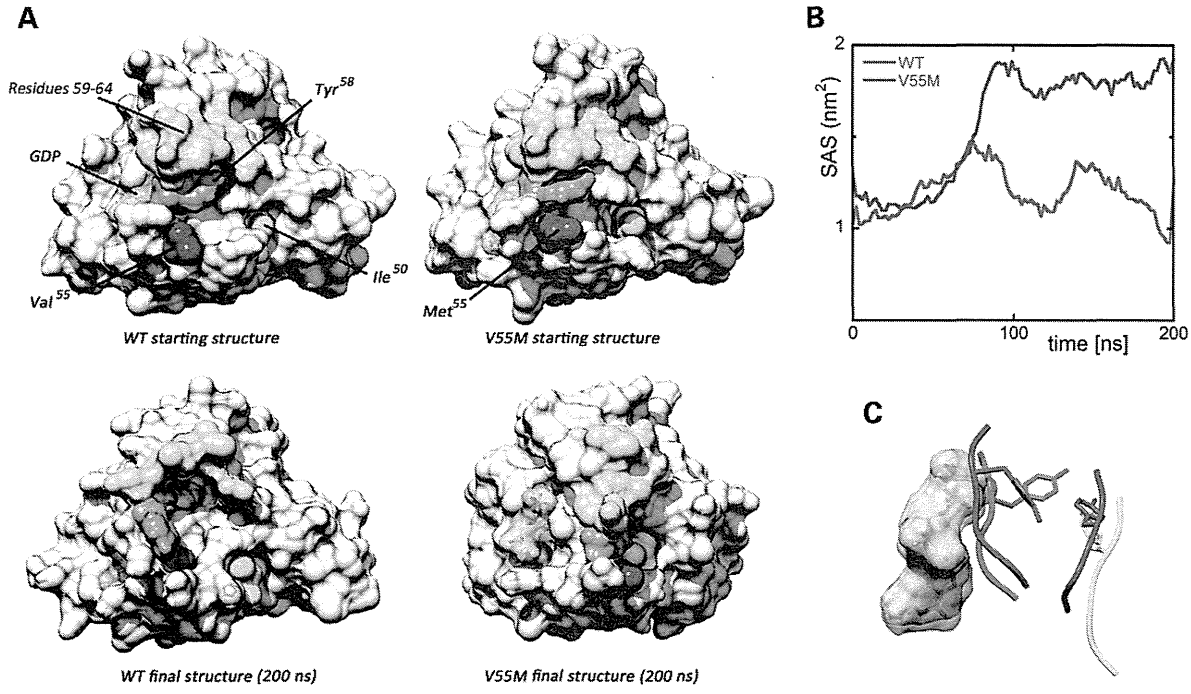

Figure 2. Molecular dynamics (MD) simulations. (**A**) Structural perturbations promoted by the p.Val55Met substitution as obtained from MD simulations of the RRAS/GDP complex. The wild-type (WT) protein is also shown for comparison. Top panels report the protein structures at the beginning of simulations, whereas the final structures (200 ns) are shown at the bottom. The final structure of $RRAS^{V55M}$ is well representative of the last 120 ns of the trajectory. The protein surface of RRAS is shown with GDP (yellow). The mutated residues and those forming a cluster in the simulation of mutated RRAS are coloured as follows: Val^{55}/Met^{55} (blue), Tyr^{58} (pink) and Ile^{50} (cyan). Residues 59–64, which, together with Tyr^{58}, form the switch I region, are coloured in green. (**B**) Solvent accessible surface of GDP in the MD simulations of wild-type (red) and mutant (blue) RRAS/GDP complexes. (**C**) Conformation of the loop comprised between Val^{55}/Met^{55} and Asp^{59} in wild-type (red) and mutant (blue) RRAS/GDP complexes obtained from MD simulations. GDP is reported as semi-transparent yellow surface. Superimposed conformations of the corresponding loop (residues 29–33) in GDP-bound HRAS (violet) (PDB: 4Q21) and GDP-bound HRAS complexed with SOS1 (cyan) (PDB: 1BKD) are shown for comparison. The side chains of Tyr^{58} and the corresponding residue in HRAS, Tyr^{32}, are displayed as sticks.

and extent of signalling through the MAPK and PI3K/AKT cascades were evaluated using transient expression in COS-7 cells. Consistent with the above-mentioned findings, pull-down assays revealed a variably higher proportion of active, GTP-bound form for both mutants (Fig. 4A). Moreover, similarly to what observed under cell-free conditions, $RRAS^{G39dup}$ was resistant to GAP stimulation. Expression of both mutants promoted enhanced serum-dependent MEK, ERK and AKT phosphorylation (Fig. 4B), which was more evident in cells expressing the $RRAS^{G39dup}$ mutant.

Caenorhabditis elegans studies

To explore further the functional impact of the RASopathy causative RRAS mutants on RAS signalling *in vivo*, we used the nematode *C. elegans* as an experimental model. In *C. elegans*, the role of *ras-1*, the *RRAS* ortholog (33), has not been characterized yet. On the contrary, proper signalling through LET-60, the *C. elegans* ortholog of RAS proteins, has been established to play a crucial role in vulval development (34). In particular, LET-60/RAS is known to mediate the priming signal (LIN-3/EGF) released by the anchor cell to induce the three nearby vulval precursor cells (VPCs), P5.p, P6.p and P7.p, to generate a normal vulva. Enhanced and decreased signalling through LET-60 and the MAPK cassette results in multiple ectopic pseudovulvae (multivulva phenotype) and a failure in VPC induction (vulvaless phenotype), respectively (34,35).

Multiple transgenic lines were generated to conditionally express the wild-type *ras-1* cDNA ($ras\text{-}1^{WT}$) or the allele homologous to the disease-associated three-nucleotide duplication ($ras\text{-}1^{G27dup}$), which was identified to occur both as a germline and somatic event. Exogenous RAS-1 expression was induced by heat shock at early L3 larval stage to investigate the effects of the mutant protein on vulval development. Animals expressing $ras\text{-}1^{G27dup}$ displayed abnormal vulval morphogenesis resulting in the formation of a protruding vulva (Pvl) (Fig. 5A and B and Supplementary Material, Table S6), a phenotype associated with aberrant traffic through different signalling cascades (36,37). Of note, this phenotype had previously been reported in worms expressing the RASopathy causative $SHOC2^{S2G}$ mutant (38). Like those animals, $ras\text{-}1^{G27dup}$ worms showed decreased egg-laying efficiency (Egl phenotype), and accumulation of larvae inside the mother (Bag-of-worms phenotype). A significantly less penetrant phenotype was observed in animals expressing $ras\text{-}1^{WT}$. These findings, together with the observation that animals lacking *ras-1* do not exhibit any vulval defect (WormBase, http://www.wormbase.org/, and our personal assessment), supported the gain-of-function role of the mutation on RAS-1 function. At the late L3/early L4 larval stage, vulva

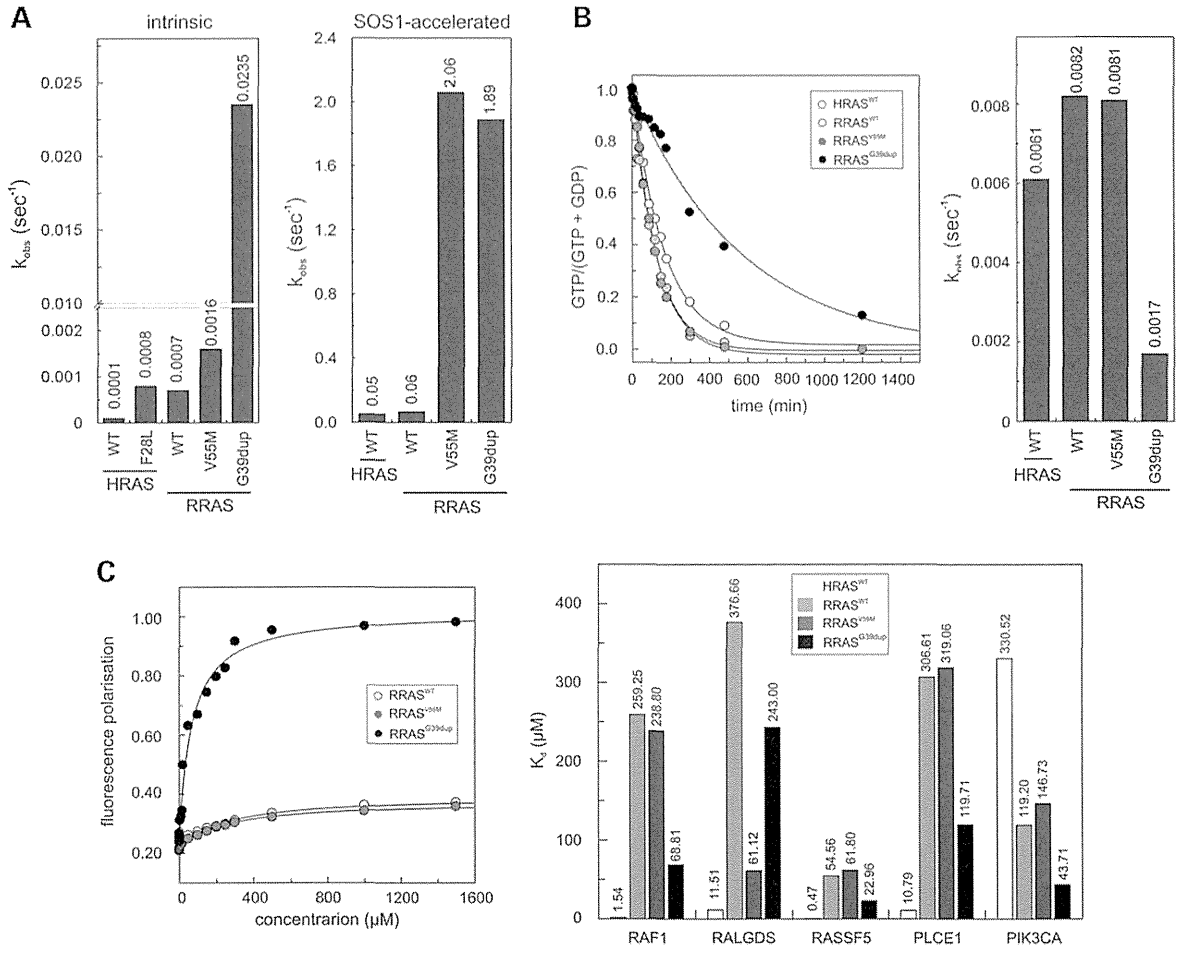

Figure 3. *In vitro* biochemical characterization of the RRAS^{G39dup} and RRAS^{V55M} mutants. (**A**) Intrinsic (left) and SOS1-accelerated (right) mantGDP nucleotide dissociation measured in the presence of 20-fold excess of non-labelled GDP. The decrease in mant fluorescence was fitted by single exponentials to obtain k_{obs} values for nucleotide dissociation. RRAS^{G39dup} exhibited a 35-fold increased intrinsic dissociation of mantGDP, whereas SOS1-accelerated mantGDP dissociation was augmented by ~30-fold for both mutants, compared with RRAS^{WT} and HRAS^{WT}. The K_{obs} values are an average of five to seven independent measurements. (**B**) Intrinsic GTP hydrolysis kinetics (left) and rate constants (right) of RRAS^{G39dup} and RRAS^{V55M} proteins, documenting the impaired catalytic activity in the former. The K_{obs} values are an average of five to seven independent measurements. (**C**) Binding of RRAS^{WT}, RRAS^{V55M} and RRAS^{G39dup} to the RAS-binding domain of RAF1 measured as variation in fluorescence polarization of each mantGppNHp-bound RRAS protein at increasing concentrations of RAF1-RBD (left), and dissociation constants (K_d) for the interaction of HRAS^{WT} and RRAS proteins to the RBDs of RAF1, RALGDS, PLCE1, PIK3CA and RASSF5 (right). K_d values were obtained by quadratic fitting of the concentration-dependent binding curves from fluorescence polarization measurement as exemplified for RAF1-RBD. Of note, RRAS^{WT} binds to RAF1, RALGDS, RASSF5 and PLCE1 less efficiently than HRAS, whereas an increased binding affinity to PIK3CA is observed.

morphogenesis normally begins with the descendants of VPC P6.p detaching from the cuticle and forming a symmetric invagination (Fig. 5C) (34). Animals in which the expression of *ras-1*^{WT} had been induced at early L3 largely maintained this pattern (17/20). In contrast, in larvae expressing *ras-1*^{G27dup}, descendants of VPCs P5.p and/or P7.p more frequently detached from the cuticle, resulting in larger and more asymmetric invaginations (10/30). This morphogenesis defect was the earliest detectable effect of the *ras-1*^{G27dup} allele on vulval development, similarly to that previously documented in transgenic lines expressing SHOC2^{S2G} (38).

Genetic interaction between the RAS-1/RRAS mutant and LET-60/RAS was also investigated. While expression of the RAS-1^{G27dup} mutant was able to exacerbate the multivulva phenotype associated with a hyperactive *let-60* allele (*n1046*), expression of wild-type RAS-1 failed to do so (Table 1). Similarly, a significant, although partial rescue of the VPC induction defect associated with a *let-23/EGFR* hypomorphic allele (*syI*) was observed in animals expressing the activating RAS-1^{G27dup} mutant, but not in worms expressing the wild-type counterpart (Table 1). Overall, these experiments provided evidence of a positive modulatory role of the RAS-1/RRAS mutant on LET-60/RAS signalling.

DISCUSSION

Mutations of genes coding for proteins with role in RAS signalling and the RAF/MEK/ERK cascade have been identified as the

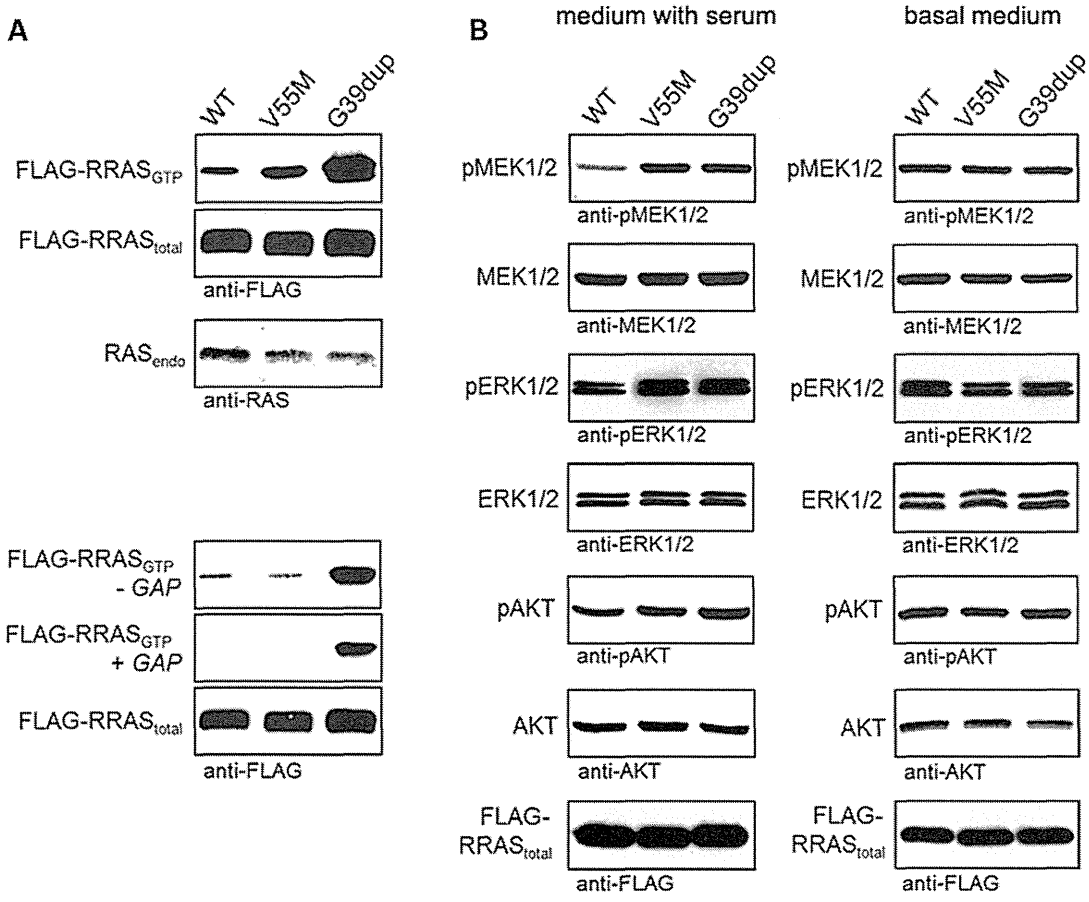

Figure 4. RRAS^{G39dup} and RRAS^{V55M} signalling activities in cells. (**A**) Determination of GTP-bound RRAS levels in COS-7 cells transiently expressing wild-type or mutant FLAG-tagged RRAS proteins. Assays were performed in the presence of serum (above), and in serum-free conditions (−GAP) or in the presence of the neurofibromin GAP domain (+GAP) (below). RRAS^{G39dup} was predominantly present in the active GTP-bound form and was resistant to GAP stimulation, whereas a slightly increased level of GTP-bound RRAS^{V55M} was observed in the presence of serum. Representative blots of three performed experiments are shown. (**B**) Determination of MEK, ERK and AKT phosphorylation levels (pMEK, pERK and pAKT) in transiently transfected COS-7 cells cultured in medium with serum (left) or basal medium (right). Expression of each RRAS mutant resulted in variably enhanced MEK, ERK and also partially AKT phosphorylation after stimulation. Total MEK, ERK and AKT in cell lysates are shown for equal protein expression and loading. Expression levels of exogenous, FLAG-tagged RRAS in cell lysates are shown for each experiment. Representative blots of three performed experiments are shown.

molecular cause underlying a group of clinically related developmental disorders, the RASopathies. Here, we used a gene candidacy approach based on large-scale protein–protein interaction/functional network analysis to identify *RRAS* as a novel gene implicated in a condition with features within the RASopathy spectrum. Disease-causing *RRAS* mutations are activating and act by maintaining the GTPase in its GTP-bound active state. Aberrant RRAS function was demonstrated to perturb variably intracellular signal flow through the RAF/MEK/ERK cascade, and to a certain extent also the PI3K/AKT pathway. Of note, these gain-of-function mutations are likely to define a novel leukaemia-prone condition. Consistent with this view, the same class of *RRAS* lesions was identified to occur as acquired somatic event in JMML, characterizing a subset of this myeloproliferative/myelodysplastic disorder with rapid progression to AML.

RRAS shares several biochemical properties with HRAS, NRAS and KRAS, as well as some common function, including stimulation of cell proliferation, survival and transformation (19,39). Despite these similarities, however, previous observations have emphasized the role of RRAS in cell adhesion, spreading and migration, and its modulatory function on effectors distinct from those used by 'classical' RAS proteins (40,41). While PI3K/AKT has been recognized as a major effector pathway of RRAS, only a minor impact on MAPK signalling had been reported (41,42). The present *in vitro* findings provide evidence that disease-associated RRAS mutants enhance the activation of the MAPK cascade, at least in response to specific stimuli. On the other hand, the identification of *RRAS* as a novel disease gene implicated in a RASopathy disorder further emphasizes the relevance of dysregulated signalling controlling cell spreading and migration in certain features of NS (e.g. congenital heart defects and lymphedema) and JMML (leukocyte infiltration in non-haematopoietic tissues) (43–45).

Caenorhabditis elegans studies provided evidence for a genetic interaction between the RAS-1^{G27dup}/RRAS^{G39dup} and

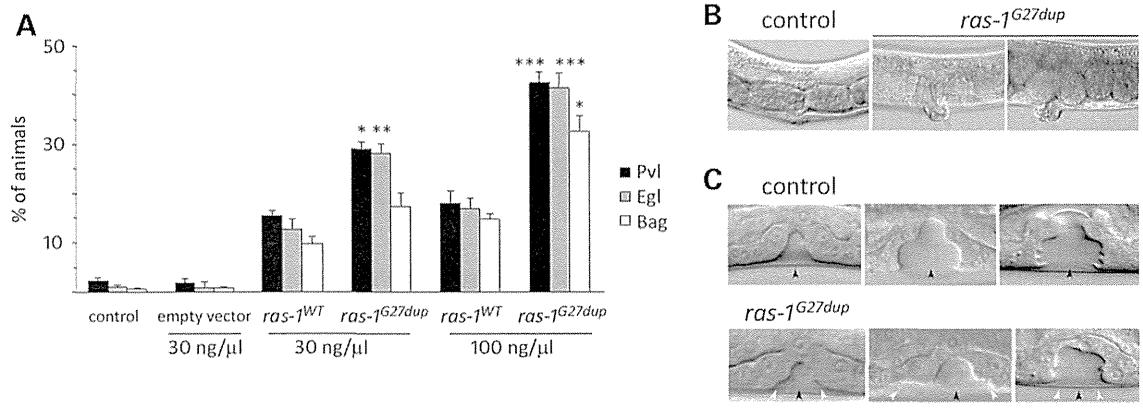

Figure 5. Consequences of *ras-1*^{G27dup} expression on *C. elegans* vulval development. (**A**) Heat-shock-driven expression of *ras-1*^{WT} and *ras-1*^{G27dup} at early L3 stage results in protruding vulva (Pvl), egg laying defective (Egl) and bag-of-worms (Bag) phenotypes. Isogenic animals that had lost the transgene (control group) and worms expressing the heat shock-inducible vector (empty vector) were subjected to heat shock and scored in parallel for comparison. The dose at which the transgene has been injected is reported at the bottom. Error bars indicate SD of three independent experiments. Asterisks indicate significant differences compared with *ras-1*^{WT} at the corresponding dose of injection ($^{*}P < 0.05$; $^{**}P < 0.005$; $^{***}P < 0.0005$; Fisher's Exact Test). (**B**) A proper vulva develops in heat-shocked control animals (left), whereas a protruding vulva is observed in heat-shocked *ras-1*^{G27dup} young adults (middle) and adult worms (right). (**C**) Nomarski images of vulval precursor cells in late L3 (left), early L4 (middle) and mid-late L4 (right) stages from synchronized animals heat-shocked at early L3. In control animals ($N = 48$), only P6.p descendants invaginate (upper panel), whereas in 10 of 30 analysed *ras-1*^{G27dup}-expressing worms, P5.p and/or P7.p descendants also detach from the cuticle, generating asymmetric invaginations (lower panel). Black arrowheads point to P6.p descendant invagination, whereas white arrowheads point to P5.p and P7.p descendant invagination. Anterior is to the left and dorsal is up, in all images.

LET-60/RAS *in vivo*. Specifically, expression of the RAS-1 mutant protein was able to rescue, in part, the VPC induction defect resulting from a hypomorphic LET-23 mutant and enhanced the multivulva phenotype associated with a LET-60 gain-of-function genetic background. No impact of wild-type RAS-1/RRAS expression was observed in both models. We also observed that worms expressing *ras-1*^{G27dup} displayed abnormal vulval morphogenesis (protruding vulva), possibly resulting from aberrant morphogenetic movements of the VPC descendant cells. Of note, we observed an equivalent phenotype in transgenic lines expressing SHOC2^{S2G} (38) and a PTPN11/SHP2 gain-of-function mutant (our unpublished data), suggesting functional equivalence of these mutants. Genetic studies support the view that these vulva defects arise, in part, through perturbation of signalling mediated by the RHO-related GTPase, RAC, which plays a critical role in vulval morphogenesis (37). This finding is in line with the established role of RRAS on RAC signalling (40,41) and with preliminary data indicating enhanced migration and chemotactic capabilities in cells stably expressing the disease-associated RRAS mutants (our unpublished data).

The biochemical characterization of disease-associated *RRAS* mutations provided strong evidence for the existence of distinct structural and mechanistic effects resulting in an overall enhancement of RRAS signalling. Function of RAS family proteins in signal transduction is controlled by two events, the GDP/GTP exchange and GTP hydrolysis. Any perturbation of these processes can affect dramatically the fine-tuned balance of the GTPase interaction with effectors and signal output. The majority of gain-of-function mutations affecting RAS proteins, including those contributing to oncogenesis, trigger the accumulation of these GTPases in the active state by impairing intrinsic GTPase activity, and/or conferring resistance to GAPs (17). This is also the case of two of the three mutations identified in this study, p.Gly39dup and p.Gln87Leu, the latter corresponding to the p.Gln61Leu in RAS proteins (present study and ref. 18,19). The characterization of the biochemical behaviour of RRAS^{G39dup}, however, also demonstrated a dramatic increase in both the intrinsic and GEF-catalysed nucleotide exchange as a process contributing to the accumulation of this mutant in its GTP-bound state. Aberrant GEF-accelerated nucleotide exchange dynamics was identified as the event driving functional dysregulation in the RRAS^{V55M} mutant, which was documented to be hyper responsive to GEF stimulation, but retained stimulus-dependency. Remarkably, the RRAS^{G39dup} and RRAS^{V55M} mutants were demonstrated to exhibit a diverse binding behaviour to effectors suggesting a differential impact of mutations on downstream signalling cascades, including PI3K/AKT and RALGDS/RAL, whose biological significance and impact, however, require further studies.

The clinical phenotype of the two subjects with germline *RRAS* mutations was reminiscent of NS. The individual with the Gly^{39} duplication displayed pulmonic stenosis, reduced growth, café-au-lait spots, mild motor delay and low-set ears, which recur in NS (5). Facial features, however, were distinctive, and not typical of NS. In contrast, the patient heterozygous for the p.Val55Met substitution exhibited a very mitigated phenotype characterized by suggestive facial characteristics (triangular face, downslanting palpebral fissures and low-set ears), low posterior hairline, broad chest and borderline cognitive abilities, without cardiac involvement or defective growth, indicating that clinical features associated with *RRAS* mutations might be quite subtle. Of note, the milder phenotype associated with the p.Val55Met change is consistent with the weaker perturbing effect of the RRAS^{V55M} mutant on MAPK and PI3K/AKT signalling compared with the RRAS^{G39dup} protein. Additional information on the spectrum of germline *RRAS* mutations, their associated phenotype and their functional impact on signalling,

Table 1. Vulva phenotypes in *C. elegans* mutant strains expressing wild-type RAS-1 or the disease-associated RAS-1^{G27dup} mutant

Genotype	Transgene	*N*	Muv (%)	Vul (%)	Pvl (%)	*N*	P6.p induction (%)
wild-type	none	207	0	0	1.0	48	100
let-60(n1046)	none	201	77.9	–	0.5	50	100
let-60(n1046)	*ras-1*^{wt}	244	76.4	–	2.8	43	100
let-60(n1046)	*ras-1*^{G27dup}	231	87.1[a]	–	3.0	50	100
let-23(sy1)	none	194	–	87.8	3.6	178	13.4
let-23(sy1)	*ras-1*^{WT}	169	–	84.3	4.1	156	14.0
let-23(sy1)	*ras-1*^{G27dup}	282	–	83.3	10.3[b]	128	24.2[c]

Strains: *let-60(n1046)* is a gain-of-function allele of *let-60* (ortholog of the human *HRAS*, *KRAS* and *NRAS* genes); *let-23(sy1)* is a hypomorphic allele of *let-23* (ortholog of the human *EGFR* gene). *ras-1*^{WT} and *ras-1*^{G27dup} indicate *hsp-16.41::ras-1*^{WT}- and *hsp-16.41::ras-1*^{G27dup}-containing constructs injected at 100 ng/μl, respectively. After each cross, isogenic worms that had lost the transgene were cloned separately and used as controls.
Animals were grown at 20°C and heat-shocked in parallel at early L3 stage. *N* indicates the number of animals scored. Multivulva (Muv), vulvaless (Vul) and protruding vulva (Pvl) phenotypes are expressed as percentage of worms with ectopic pseudovulvae, animals lacking a vulva and adults with a protruding vulva, respectively. Induction of vulval cell fate is expressed as percentage of P6.p that has been induced to invaginate.
In all comparisons, *P*-values were calculated using two-tailed Fisher's exact test.
[a]Significantly different from *let-60(n1046)* ($P < 0.02$).
[b]Significantly different from *let-23(sy1)* ($P < 0.01$) and *let-23(sy1);ras-1*^{WT} ($P < 0.02$).
[c]Significantly different from *let-23(sy1)* ($P = 0.02$) and *let-23(sy1);ras-1*^{WT} ($P < 0.05$).

however, is necessary to establish clinically relevant genotype–phenotype correlations.

JMML is a clonal myeloproliferative/myelodysplastic disorder of childhood characterized by overproduction of immature myeloid cells that variably retain the capacity to differentiate. Upregulation of RAS/MAPK signalling owing to germline and somatic mutations in *PTPN11*, *NRAS*, *KRAS*, *NF1* and *CBL* is a major event implicated in this malignancy (13,46,47). Our data document that upregulated RRAS function represents a novel event contributing to JMML pathogenesis and/or disease progression. Notably, somatic *RRAS* mutations co-occurred with acquired *NRAS* lesions in atypical JMML characterized by late onset and rapid progression to AML. While JMML is generally an aggressive malignancy, a subset of *NRAS/KRAS* mutation-positive patients has been reported to exhibit a mild course, with spontaneous remission despite the *RAS*-mutated clone persisting for years (48–50, our unpublished data). This suggests that in some instances, certain *NRAS* mutations are not sufficient to support full leukaemogenesis, requiring synergism with a second RAS signalling targeting event. In line with this view, *NRAS* mutations have been documented to co-exist with defects in other RASopathy genes (e.g. *PTPN11*) in some cases resulting in a particularly aggressive disease resembling AML with myelodysplasia-related changes (51,52), as that observed in the present cases. Other studies, however, are required to appreciate more precisely the role of enhanced RRAS function in leukaemogenesis as well as its clinical relevance in haematological malignancies.

In conclusion, our findings document that germline activating mutations in *RRAS* underlie a condition within the RASopathy family that may resemble NS phenotypically. In the examined cohorts, *RRAS* lesions were found to account for only a small portion of cases, which might be related to their severe consequences on embryonic/foetal development and/or to the biased selection of the subjects included in this study. Based on the present findings, however, *RRAS* mutations are expected to be more common among subjects with clinical features only partially overlapping NS, and particularly in patients with syndromic JMML/AML not associated with mutations in the *PTPN11*, *NF1*, *CBL*, *KRAS* and *NRAS* genes. While further efforts are required to characterize more precisely the clinical impact of germline and somatic mutations affecting *RRAS*, our findings suggest an unpredicted role of this GTPase in development and haematopoiesis. Consistent with the recent identification of *RIT1* as disease gene implicated in a significant proportion of NS (9), our findings further extend the concept of 'RASopathy gene' to a transducer whose dysregulated function perturbs signal flow through the MAPK cascade but does not belong to the core RAS/MAPK signalling cassette.

MATERIALS AND METHODS

Selection of RASopathy candidate genes

A web-based tool, Genes2FANs (http://actin.pharm.mssm.edu/genes2FANs), using a large-scale protein–protein interaction network coupled to a panel of functional association networks (FANs) was utilized to build a subnetwork connecting proteins to the known RASopathy genes (i.e. *PTPN11*, *SOS1*, *NF1*, *SPRED1*, *CBL*, *NRAS*, *KRAS*, *HRAS*, *RAF1*, *BRAF*, *SHOC2*, *MAP2K1* and *MAP2K2*), as seed proteins. Gene Ontology (biological process tree), mammalian phenotype browser, and Connectivity Map (drug-associated gene expression signatures), ChEA and TRANSFAC (transcription factor networks) databases were selected to construct the functional subnetworks utilized for prioritization of candidates (15). The programme allows to calculate z-scores for intermediate nodes (i.e. candidates), which are ranked based on their connections to the seed proteins.

Subjects and mutation analysis

Three cohorts of patients were considered in the study. A first group including 96 subjects with clinical features within the RASopathy spectrum and without mutation in previously identified RASopathy genes (i.e. *CBL*, *PTPN11*, *SOS1*, *KRAS*, *HRAS*, *NRAS*, *RAF1*, *BRAF*, *SHOC2*, *MAP2K1* and *MAP2K2*) was screened for a selected panel of candidates. A second cohort including 408 subjects with NS or a closely related phenotype previously tested negative for mutations in a heterogeneous subset

of RASopathy genes was scanned for *RRAS* mutations. All subjects included in this cohort had been screened for mutations in *PTPN11*, *SOS1* and *RAF1* genes. In both cohorts, the clinical diagnosis was made on the basis of standardized clinical criteria assessed by experienced clinical geneticists and paediatricians. Clinical features for the majority of subjects satisfied diagnostic criteria reported for NS, LEOPARD syndrome and cardiofaciocutaneous syndrome (53–57), but individuals who lacked sufficient features for a definitive diagnosis were also included. *RRAS* mutation analysis was also carried out on a cohort including 110 subjects with non-syndromic JMML that had prospectively been collected and genotyped (58). Mutation screening was performed on the entire *RRAS* coding sequence and flanking intronic stretches (NC_000019.10, 49635295.. 49640143, complement; NM_006270.3; NP_006261.1) on genomic DNA extracted from circulating leukocytes (cohorts I, II and III) or bone marrow aspirates (cohort III) by denaturing high-performance liquid chromatography (DHPLC) (3100 or 3500HT WAVE DNA fragment analysis system, Transgenomic, Omaha, NE, USA) and/or direct bidirectional sequencing (ABI Prism 3130, 3730 and 3500 Genetic Analyzers; Applied Biosystems, Foster City, CA, USA). Primer pairs, PCR and DHPLC conditions are available upon request. dbSNP137 (http://www.ncbi.nlm.nih.gov/projects/SNP/snp_summary.cgi), HapMap (rel.27) (http://hapmap.ncbi.nlm.nih.gov/) and 1000 Genomes (http://www.1000genomes.org/) databases were used to annotate the identified sequence variants. SIFT (http://sift.jcvi.org/), PolyPhen-2 (http://genetics.bwh.harvard.edu/pph2/) and MutationTaster (http://www.mutationtaster.org/) were used to predict the functional impact of the identified variants. Paternity was confirmed by STR genotyping, using the PowerPlex 16 System (Promega). DNA from leukocytes, hair bulb cells, bone marrow aspirates and skin fibroblasts was extracted using standard protocols. DNA specimens were collected under Institutional Review Board-approved protocols. Informed consent for DNA storage and genetic analyses was obtained from all subjects. Permission was obtained to publish picture of patient 9802, whereas subject NS1166 denied consent for picture publication.

Exome sequencing

Targeted enrichment and massively parallel sequencing were performed on genomic DNA extracted from circulating leukocytes and fibroblasts of patient 9802. Exome capture was carried out using the SureSelect Human All Exon V4+UTRs (Agilent), and sequencing with a HiSeq2000 instrument (Illumina). Image analysis and base calling were performed using the Real Time Analysis (RTA) pipeline v. 1.14 (Illumina). Paired-end reads alignment to the reference human genome (UCSC GRCh37/hg19) and variant calling were carried out using the CASAVA v. 1.8 pipeline (Illumina). Variant annotation, SNP filtering (dbSNP135, 1000 Genomes, HapMap and IntegraGen Exome databases) and patient-matched germline variant filtering were attained using an in-house pipeline by IntegraGen (Evry, France).

Molecular dynamics analyses

Starting coordinates for MD simulations were obtained from the RRAS crystallographic structure in complex with GDP and Mg^{2+} (PDB: 2FN4; RCSB Protein Data Bank, http://www.rcsb.org/pdb/home/home.do). The *N*-terminus and *C*-terminus of RRAS, absent in the crystal, were not considered in simulations. Deep View software was used to add atoms missing in the PDB file, belonging to residues 31, 96, 114, 121 and 192 as well as to substitute residue 55 (simulation of the p.Val55Met mutant) (59). All MD simulations were performed with GROMACS 4.5 package, by using the GROMOS96 43a1 force field parameters for the protein. Parameters for GDP were taken from the GROMACS website (http://www.gromacs.org). Simulations were performed as previously described (60,61), except for some details. Briefly, the proteins were initially placed in a dodecahedral box, solvated with ~6700 SPC water molecules, and six Na^+ ions were added to neutralize the protein charge. Following initial energy minimization and a 100-ps MD run, during which the protein atoms were position restrained, the temperature of solute and solvent was raised from 50 to 300 K in a stepwise manner. 200-ns-long simulations were performed for wild-type RRAS and the RASopathy causative mutant. The particle mesh Ewald method was used to evaluate electrostatic interactions (62), whereas a cut-off scheme was employed for Van der Waals interactions. Temperature and pressure were kept constant at 300 K and 1 bar by using the Berendsen weak-coupling method (63), using separate temperature baths for protein–GDP complex and solvent, with a relaxation time of 0.1 ps for temperature and 1 ps for pressure. A time step of 2 fs was employed. Root mean square deviations were calculated according to standard definitions. UCSF Chimera (http://www.cgl.ucsf.edu/chimera/) was used for molecular graphics and structures superposition, by using the MatchMaker option.

Biochemical and functional characterization of RRAS mutants

The generation of constructs, and preparation and purification of proteins were as previously described (64). The intrinsic activities of the RAS proteins, their modulation by GEFs and GAPs and their interaction with different effector proteins were determined as described earlier (65,66). Dissociation of mantGDP from RAS proteins (0.1 μM) was measured in the presence of 20 μM GDP in 30 mM Tris–HCl, pH 7.5, 10 mM KH_2PO_4/K_2HPO_4, 5 mM $MgCl_2$, 3 mM dithioerythritol (DTE), at 25 °C, using a Perkin Elmer fluorimeter at 366 nm (excitation wavelength) and 450 nm (emission wavelength). Observed rate constants (k_{obs}) of dissociation were obtained by single exponential fitting of the data. GEF-accelerated mantGDP dissociation from RAS proteins (0.1 μM) was measured as mentioned earlier, in the presence of the catalytic domain of SOS1, Cdc25 (5 μM), using stopped-flow instrument.

The intrinsic GTPase reaction was performed by mixing 70 μM nucleotide-free RAS proteins (HRAS, $RRAS^{WT}$, $RRAS^{V55M}$ and $RRAS^{G39dup}$) with 50 μM GTP in 30 mM Tris–HCl, pH 7.5, 10 mM KH_2PO_4/K_2HPO_4, 10 mM $MgCl_2$, 3 mM DTE, at 25°C, using HPLC assay as previously described (67). Samples were taken at different time points and analysed by HPLC for their GDP and GTP contents to determine the relative GTP content [(GTP)/(GDP + GTP)]. Intrinsic GTP hydrolysis k_{obs} of proteins were obtained by single exponential fitting of the data. For determination of GAP (neurofibromin, residues

1–333)-stimulated GTPase activity, GDP bound to HRAS and RRAS proteins was exchanged with excess mantGTP in the presence of alkaline phosphatase. Unbound nucleotides were removed by NAP5 column, and the RAS/mantGTP proteins were snap-frozen in liquid nitrogen (66). GAP-stimulated GTP hydrolysis of RAS proteins (0.2 μM) was measured in 30 mM Tris–HCl, pH 7.5, 10 mM $MgCl_2$, 3 mM DTE at 25°C using a Hightech TgK Scientific stopped-flow instrument. Reactions measured the decrease in fluorescence owing to hydrolysis of mantGTP. This decay was fit by a single exponential.

Effector binding assays were performed in 30 mM Tris–HCl, pH 7.5, 100 mM NaCl, 5 mM $MgCl_2$, 3 mM DTE at 25°C using a Fluoromax 4 fluorimeter in polarization mode. Increasing amounts of GST-tagged RAS-binding domains (RBD) of RAS effectors were titrated to 0.3 μM mantGppNHp-bound RAS proteins resulting in an increase of polarization (64). The dissociation constants (K_d) were calculated by fitting the concentration-dependent binding curve using a quadratic ligand binding equation.

For cell-based assays, COS-7 cells were transiently transfected with FLAG-tagged $RRAS^{WT}$, $RRAS^{V55M}$ or $RRAS^{G39dup}$ by the DEAE-dextran method. For serum conditions, cells were incubated for 48 h in 10% FCS. In serum-starved conditions, serum was changed to basal medium midway between the transfection and harvesting. Transfected COS-7 cells were harvested and lysed in fishing buffer [50 mM Tris–HCl, pH 7.5, 2 mM $MgCl_2$, 100 mM NaCl, 1% IGEPAL CA-630, 10% glycerol, EDTA-free protease inhibitor cocktail (Roche, 1 tablet/50 ml buffer), 20 mM disodium β-glycerol phosphate and 1 mM Na_3VO_4]. Cleared cell lysates were incubated with GSH-beads loaded with GST-RAF1-RBD. GTP-bound proteins and total recombinant proteins were analysed by immunoblotting with anti-FLAG antibody. Antibodies against MEK1/2, ERK1/2, AKT, phospho-MEK1/2 (Ser217/221), phospho-ERK1/2 (Thr202/Tyr204) and phospho-AKT (Thr308) were purchased from Cell Signaling Technology (68).

Caenorhabditis elegans studies

Culture and maintenance of animals were as previously described (69). The *let-60(n1046)* (*let-60/RAS* gain-of-function allele) and *let-23(sy1)* (*let-23/EGFR* hypomorphic allele) strains were provided by the *Caenorhabditis Genetics Center* (University of Minnesota). The three-nucleotide insertion, c.81_82insGGC (*ras-1^{G27dup}*), corresponding to c.116_118dup in *RRAS*, was introduced in the wild-type cDNA (*ras-1^{WT}*) (*C. elegans* ORF clone AAB03320, Thermo Scientific) by site-directed mutagenesis (QuikChange Site-Directed Mutagenesis Kit, Stratagene). *ras-1* cDNAs were subcloned into the pPD49.83 heat shock-inducible vector (a gift of A. Fire, Stanford University School of Medicine). Germline transformation was performed as described (70). pJM371 plasmid [*pelt-2*::NLS::*RFP*] (a gift from J.D. McGhee, University of Calgary), which drives red fluorescent protein (RFP) expression in intestinal cell nuclei, was used as co-injection marker (30 ng/μl). Two different doses of constructs were injected (30 and 100 ng/μl). Animals from at least three independent transgenic lines for each construct and each dose of injection (i.e. six lines expressing *ras-1^{WT}* and six lines expressing *ras-1^{G27dup}*) were heat-shocked in parallel and scored blindly at a Leica MZ10F dissecting microscope to check for the presence of protruding vulvae (Pvl phenotype) and multiple ectopic pseudovulvae (Muv phenotype), count the number of eggs retained in the uterus (Egl phenotype) and identify animals that had become bag-of-worms (Bag phenotype). Isogenic worms that had lost the transgene were cloned separately and used as controls. Following heat shock, all the transgenic lines expressing *ras-1^{WT}* or *ras-1^{G27dup}* showed a variable degree of these phenotypes. Lines *gbEx555a*[*hsp-16.41*::*ras-1^{WT}*;*pelt-2*::NLS::*RFP*] and *gbEx557a*[*hsp-16.41*::*ras-1^{G27dup}*;*pelt-2*::NLS::*RFP*] were scored quantitatively in triplicate experiments at the compound microscope and used for further analyses. Genetic crosses were performed according to standard methods (69). The genotype of individual alleles was confirmed by direct sequencing of the appropriate genomic region. After each cross, isogenic worms that had lost the transgene were used as controls.

To investigate VPCs induction and vulva morphogenesis, synchronized hermaphrodites carrying each transgene and the corresponding isogenic controls were heat-shocked in parallel at early L3 stage (33°C, 1 h, followed by 30°C, 1 h). Animals were scored at the compound microscope for vulval induction at late L3 and L4 stages, and for Pvl/Egl/Bag phenotypes at the adult stage. Microscopy observations were performed with a Nikon Eclipse 80i instrument equipped with Nomarski differential interference contrast optics on live animals mounted on 2% agarose pads containing 10 mM sodium azide as anaesthetic.

SUPPLEMENTARY MATERIAL

Supplementary Material is available at *HMG* online.

ACKNOWLEDGEMENTS

We are grateful to the participating patients and their families. We thank Serenella Venanzi (Istituto Superiore di Sanità, Rome, Italy), Michela Bonaguro (Policlinico S.Orsola-Malpighi, Bologna, Italy), Federica Consoli (Istituto Mendel, Rome, Italy) and Cédric Vignal and Sabrina Pereira (Hôpital Robert Debré, Paris, France) for skilful technical assistance, and the Open Laboratory (IGB-CNR, Naples, Italy) for experimental support. We also thank Paolo Bazzicalupo (IGB-CNR) for critical reading of the manuscript, paediatricians from the *Société Française des Cancers de l'Enfant* (SFCE) for providing biological material from their patients and CINECA for computational resources. Some nematode strains used in this work were provided by the *Caenorhabditis Genetics Center* (University of Minnesota, Minneapolis, MN, USA) funded by the NIH Office of Research Infrastructure Programs (P40OD010440).

Conflict of Interest statement. None declared.

FUNDING

This work was supported by grants from the ERA-Net for research programmes on rare diseases 2009 (NSEuroNet to M.Z., H.C., M.R.A. and M.T.), Telethon-Italy (GGP10020 and GGP13107 to M.T.), AIRC (IG 13360 to M.T.), NGFNplus program of the German Ministry of Science and Education (01GS08100 to M.R.A.), German Research Foundation through the Collaborative Research Center 974 (Communication and Systems Relevance

during Liver Injury and Regeneration to M.R.A.) and NIH (HL071207 to B.D.G.). F.P. was recipient of a research fellowship from '*Associazione Italiana Sindromi di Costello e cardiofaciocutanea*'. Funding to pay the Open Access publication charges for this article was provided by Telethon-Italy.

REFERENCES

1. Mitin, N., Rossman, K.L. and Der, C.J. (2005) Signaling interplay in Ras superfamily function. *Curr. Biol.*, **15**, R563–R574.
2. Mendoza, M.C., Er, E.E. and Blenis, J. (2011) The Ras-ERK and PI3K-mTOR pathways: cross-talk and compensation. *Trends Biochem. Sci.*, **36**, 320–328.
3. Harris, T.J.R. and McCormick, F. (2010) The molecular pathology of cancer. *Nat. Rev. Clin. Oncol.*, **7**, 251–265.
4. Pylayeva-Gupta, Y., Grabocka, E. and Bar-Sagi, D. (2011) RAS oncogenes: weaving a tumorigenic web. *Nat. Rev. Cancer*, **11**, 761–774.
5. Roberts, A.E., Allanson, J.E., Tartaglia, M. and Gelb, B.D. (2013) Noonan syndrome. *Lancet*, **381**, 333–342.
6. Schubbert, S., Shannon, K. and Bollag, G. (2007) Hyperactive Ras in developmental disorders and cancer. *Nat. Rev. Cancer*, **7**, 295–308.
7. Tartaglia, M. and Gelb, B.D. (2010) Disorders of dysregulated signal traffic through the RAS-MAPK pathway: phenotypic spectrum and molecular mechanisms. *Ann. N. Y. Acad. Sci.*, **1214**, 99–121.
8. Rauen, K.A. (2013) The RASopathies. *Annu. Rev. Genomics Hum. Genet.*, **14**, 355–369.
9. Aoki, Y., Niihori, T., Banjo, T., Okamoto, N., Mizuno, S., Kurosawa, K., Ogata, T., Takada, F., Yano, M., Ando, T. *et al.* (2013) Gain-of-function mutations in RIT1 cause Noonan syndrome, a RAS/MAPK pathway syndrome. *Am. J. Hum. Genet.*, **93**, 173–180.
10. Tartaglia, M., Gelb, B.D. and Zenker, M. (2011) Noonan syndrome and clinically related disorders. *Best Pract. Res. Clin. Endocrinol. Metab.*, **25**, 161–179.
11. Kratz, C.P., Rapisuwon, S., Reed, H., Hasle, H. and Rosenberg, P.S. (2011) Cancer in Noonan, Costello, cardiofaciocutaneous and LEOPARD syndromes. *Am. J. Med. Genet. C Semin. Med. Genet.*, **157C**, 83–89.
12. Gripp, K.W. (2005) Tumor predisposition in Costello syndrome. *Am. J. Med. Genet. C Semin. Med. Genet.*, **137C**, 72–77.
13. Loh, M.L. (2011) Recent advances in the pathogenesis and treatment of juvenile myelomonocytic leukaemia. *Br. J. Haematol.*, **152**, 677–687.
14. McKay, M.M. and Morrison, D.K. (2007) Integrating signals from RTKs to ERK/MAPK. *Oncogene*, **26**, 3113–3121.
15. Dannenfelser, R., Clark, N.R. and Ma'ayan, A. (2012) Genes2FANs: connecting genes through functional association networks. *BMC Bioinformatics*, **13**, 156.
16. Lowe, D.G., Capon, D.J., Delwart, E., Sakaguchi, A.Y., Naylor, S.L. and Goeddel, D.V. (1987) Structure of the human and murine R-ras genes, novel genes closely related to ras proto-oncogenes. *Cell*, **48**, 137–146.
17. Wennerberg, K., Rossman, K.L. and Der, C.J. (2005) The Ras superfamily at a glance. *J. Cell Sci.*, **118**, 843–846.
18. Krengel, U., Schlichting, I., Scherer, A., Schumann, R., Frech, M., John, J., Kabsch, W., Pai, E.F. and Wittinghofer, A. (1990) Three-dimensional structures of H-ras p21 mutants: molecular basis for their inability to function as signal switch molecules. *Cell*, **62**, 539–548.
19. Saez, R., Chan, A.M., Miki, T. and Aaronson, S.A. (1994) Oncogenic activation of human R-ras by point mutations analogous to those of prototype H-ras oncogenes. *Oncogene*, **9**, 2977–2982.
20. Aoki, Y., Niihori, T., Kawame, H., Kurosawa, K., Ohashi, H., Tanaka, Y., Filocamo, M., Kato, K., Suzuki, Y., Kure, S. *et al.* (2005) Germline mutations in HRAS proto-oncogene cause Costello syndrome. *Nat. Genet.*, **37**, 1038–1040.
21. Bollag, G., Adler, F., elMasry, N., McCabe, P.C., Conner, E. Jr, Thompson, P., McCormick, F. and Shannon, K. (1996) Biochemical characterization of a novel KRAS insertion mutation from a human leukemia. *J. Biol. Chem.*, **271**, 32491–32494.
22. Reimann, C., Arola, M., Bierings, M., Karow, A., van den Heuvel-Eibrink, M.M., Hasle, H., Niemeyer, C.M. and Kratz, C.P. (2006) A novel somatic K-Ras mutation in juvenile myelomonocytic leukemia. *Leukaemia*, **20**, 1637–1638.
23. Murugan, A.K., Hong, N.T., Cuc, T.T., Hung, N.C., Munirajan, A.K., Ikeda, M.A. and Tsuchida, N. (2009) Detection of two novel mutations and relatively high incidence of H-RAS mutations in Vietnamese oral cancer. *Oral. Oncol.*, **45**, e161–e166.
24. Sartori, G., Cavazza, A., Sgambato, A., Marchioni, A., Barbieri, F., Longo, L., Bavieri, M., Murer, B., Meschiari, E., Tamberi, S. *et al.* (2009) EGFR and K-ras mutations along the spectrum of pulmonary epithelial tumors of the lung and elaboration of a combined clinicopathologic and molecular scoring system to predict clinical responsiveness to EGFR inhibitors. *Am. J. Clin. Pathol.*, **131**, 478–489.
25. Milburn, M.V., Tong, L., deVos, A.M., Brünger, A., Yamaizumi, Z., Nishimura, S. and Kim, S.-H. (1990) Molecular switch for signal transduction: structural differences between active and inactive forms of protooncogenic ras proteins. *Science*, **247**, 939–945.
26. Diaz, J.F., Wroblowski, B., Schlitter, J. and Engelborghs, Y. (1997) Calculation of pathways for the conformational transition between the GTP- and GDP-bound states of the Ha-ras-p21 protein: calculations with explicit solvent simulations and comparison with calculations in vacuum. *Proteins*, **28**, 434–451.
27. Kuppens, S., Díaz, J.F. and Engelborghs, Y. (1999) Characterization of the hinges of the effector loop in the reaction pathway of the activation of ras-proteins. Kinetics of binding of beryllium trifluoride to V29G and I36G mutants of Ha-ras-p21. *Prot. Sci.*, **8**, 1860–1866.
28. Ma, J. and Karplus, M. (1997) Molecular switch in signal transduction: reaction paths of the conformational changes in ras p21. *Proc. Natl. Acad. Sci. USA*, **94**, 11905–11910.
29. Gorfe, A.A., Grant, B.J. and McCammon, J.A. (2008) Mapping the nucleotide and isoform-dependent structural and dynamical features of Ras proteins. *Structure*, **16**, 885–896.
30. Hall, B.E., Yang, S.S., Boriack-Sjodin, P.A., Kuriyan, J. and Bar-Sagi, D. (2001) Structure-based mutagenesis reveals distinct functions for Ras switch 1 and switch 2 in Sos-catalyzed guanine nucleotide exchange. *J. Biol. Chem.*, **276**, 27629–27637.
31. Suzuki, J., Kaziro, Y. and Koide, H. (1997) An activated mutant of R-Ras inhibits cell death caused by cytokine deprivation in BaF3 cells in the presence of IGF-I. *Oncogene*, **15**, 1689–1697.
32. Scheffzek, K., Ahmadian, M.R., Kabsch, W., Wiesmüller, L., Lautwein, A., Schmitz, F. and Wittinghofer, A. (1997) The Ras-RasGAP complex: structural basis for GTPase activation and its loss in oncogenic Ras mutants. *Science*, **277**, 333–338.
33. Lundquist, E.A. (2006) Small GTPases. In *WormBook*. The *C. elegans* Research Community, WormBook (ed.), http://www.wormbook.org. doi:/10.1895/wormbook.1.67.1.
34. Sternberg, P.W. (2005) Vulval development. In *Wormbook*. The *C. elegans* Research Community (ed.), http://www.wormbook.org. doi:10.1895/wormbook.1.6.1.
35. Sundaram, M.V. (2006) RTK/Ras/MAPK signaling. In *Wormbook*. The *C. elegans* Research Community (ed.), http://www.wormbook.org. doi/10.1895/wormbook.1.80.1.
36. Eisenmann, D.M. and Kim, S.K. (2000) Protruding vulva mutants identify novel loci and Wnt signaling factors that function during *Caenorhabditis elegans* vulva development. *Genetics*, **156**, 1097–1116.
37. Kishore, R.S. and Sundaram, M.V. (2002) ced-10 Rac and mig-2 function redundantly and act with unc-73 trio to control the orientation of vulval cell divisions and migrations in *Caenorhabditis elegans*. *Dev. Biol.*, **241**, 339–348.
38. Cordeddu, V., Di Schiavi, E., Pennacchio, L.A., Ma'ayan, A., Sarkozy, A., Fodale, V., Cecchetti, S., Cardinale, A., Martin, J., Schackwitz, W. *et al.* (2009) Mutation of SHOC2 promotes aberrant protein N-myristoylation and causes Noonan-like syndrome with loose anagen hair. *Nat. Genet.*, **41**, 1022–1026.
39. Cox, A.D., Brtva, T.R., Lowe, D.G. and Der, C.J. (1994) R-Ras induces malignant, but not morphologic, transformation of NIH3T3 cells. *Oncogene*, **9**, 3281–3288.
40. Wozniak, M.A., Kwong, L., Chodniewicz, D., Klemke, R.L. and Keely, P.J. (2005) R-Ras controls membrane protrusion and cell migration through the spatial regulation of Rac and Rho. *Mol. Biol. Cell*, **16**, 84–96.
41. Osada, M., Tolkacheva, T., Li, W., Chan, T.O., Tsichlis, P.N., Saez, R., Kimmelman, A.C. and Chan, A.M. (1999) Differential roles of Akt, Rac, and Ral in R-Ras-mediated cellular transformation, adhesion, and survival. *Mol. Cell. Biol.*, **19**, 6333–6344.
42. Marte, B.M., Rodriguez-Viciana, P., Wennström, S., Warne, P.H. and Downward, J. (1997) R-Ras can activate the phosphoinositide 3-kinase but not the MAP kinase arm of the Ras effector pathways. *Curr. Biol.*, **7**, 63–70.

43. Jopling, C., van Geemen, D. and den Hertog, J. (2007) Shp2 knockdown and Noonan/LEOPARD mutant Shp2-induced gastrulation defects. *PLoS Genet.*, **3**, e225.
44. Wang, S., Yu, W.M., Zhang, W., McCrae, K.R., Neel, B.G. and Qu, C.K. (2009) Noonan syndrome/leukemia-associated gain-of-function mutations in SHP-2 phosphatase (PTPN11) enhance cell migration and angiogenesis. *J. Biol. Chem.*, **284**, 913–920.
45. Chen, P.C., Wakimoto, H., Conner, D., Araki, T., Yuan, T., Roberts, A., Seidman, C., Bronson, R., Neel, B., Seidman, J.G. *et al.* (2010) Activation of multiple signalling pathways causes developmental defects in mice with a Noonan syndrome-associated Sos1 mutation. *J. Clin. Invest.*, **120**, 4353–4365.
46. Emanuel, P.D. (2008) Juvenile myelomonocytic leukemia and chronic myelomonocytic leukemia. *Leukemia*, **22**, 1335–1342.
47. Niemeyer, C.M. and Kratz, C.P. (2008) Paediatric myelodysplastic syndromes and juvenile myelomonocytic leukaemia: molecular classification and treatment options. *Br. J. Haematol.*, **140**, 610–624.
48. Matsuda, K., Shimada, A., Yoshida, N., Ogawa, A., Watanabe, A., Yajima, S., Iizuka, S., Koike, K., Yanai, F., Kawasaki, K. *et al.* (2007) Spontaneous improvement of hematologic abnormalities in patients having juvenile myelomonocytic leukemia with specific RAS mutations. *Blood*, **109**, 5477–5480.
49. Flotho, C., Kratz, C.P., Bergsträsser, E., Hasle, H., Starý, J., Trebo, M., van den Heuvel-Eibrink, M.M., Wójcik, D., Zecca, M., Locatelli, F. *et al.* (2008) Genotype-phenotype correlation in cases of juvenile myelomonocytic leukemia with clonal RAS mutations. *Blood*, **111**, 966–967.
50. Takagi, M., Piao, J., Lin, L., Kawaguchi, H., Imai, C., Ogawa, A., Watanabe, A., Akiyama, K., Kobayashi, C., Mori, M. *et al.* (2013) Autoimmunity and persistent RAS-mutated clones long after the spontaneous regression of JMML. *Leukaemia*, **27**, 1926–1928.
51. Park, H.D., Lee, S.H., Sung, K.W., Koo, H.H., Jung, N.G., Cho, B., Kim, H.K., Park, I.A., Lee, K.O., Ki, C.S. *et al.* (2012) Gene mutations in the Ras pathway and the prognostic implication in Korean patients with juvenile myelomonocytic leukemia. *Ann. Hematol.*, **91**, 511–517.
52. Sakaguchi, H., Okuno, Y., Muramatsu, H., Yoshida, K., Shiraishi, Y., Takahashi, M., Kon, A., Sanada, M., Chiba, K., Tanaka, H. *et al.* (2013) Exome sequencing identifies secondary mutations of SETBP1 and JAK3 in juvenile myelomonocytic leukemia. *Nat. Genet.*, **45**, 937–941.
53. Van der Burgt, I., Berends, E., Lommen, E., van Beersum, S., Hamel, B. and Mariman, E. (1994) Clinical and molecular studies in a large Dutch family with Noonan syndrome. *Am. J. Med. Genet.*, **53**, 187–191.
54. Allanson, J.E. (1987) Noonan syndrome. *J. Med. Genet.*, **24**, 9–13.
55. Sarkozy, A., Digilio, M.C. and Dallapiccola, B. (2008) LEOPARD syndrome. *Orphanet J. Rare Dis.*, **3**, 13.
56. Voron, D.A., Hatfield, H.H. and Kalkhoff, R.K. (1976) Multiple lentigines syndrome: case report and review of the literature. *Am. J. Med.*, **60**, 447–456.
57. Roberts, A., Allanson, J., Jadico, S.K., Kavamura, M.I., Noonan, J., Opitz, J.M., Young, T. and Neri, G. (2006) The cardiofaciocutaneous syndrome. *J. Med. Genet.*, **43**, 833–842.
58. Pérez, B., Kosmider, O., Cassinat, B., Renneville, A., Lachenaud, J., Kaltenbach, S., Bertrand, Y., Baruchel, A., Chomienne, C., Fontenay, M. *et al.* (2010) Genetic typing of CBL, ASXL1, RUNX1, TET2 and JAK2 in juvenile myelomonocytic leukaemia reveals a genetic profile distinct from chronic myelomonocytic leukaemia. *Br. J. Haematol.*, **151**, 460–468.
59. Guex, N. and Peitsch, M.C. (1997) SWISS-MODEL and the Swiss-PdbViewer: an environment for comparative protein modeling. *Electrophoresis*, **18**, 2714–2723.
60. Martinelli, S., Torreri, P., Tinti, M., Stella, L., Bocchinfuso, G., Flex, E., Grottesi, A., Ceccarini, M., Palleschi, A., Cesareni, G. *et al.* (2008) Diverse driving forces underlie the invariant occurrence of the T42A, E139D, I282V and T468M SHP2 amino acid substitutions causing Noonan and LEOPARD syndromes. *Hum. Mol. Genet.*, **17**, 2018–2029.
61. Bocchinfuso, G., Stella, L., Martinelli, S., Flex, E., Carta, C., Pantaleoni, F., Pispisa, B., Venanzi, M., Tartaglia, M. and Palleschi, A. (2007) Structural and functional effects of disease-causing amino acid substitutions affecting residues Ala72 and Glu76 of the protein tyrosine phosphatase SHP-2. *Proteins*, **66**, 963–974.
62. Darden, T., York, D. and Pedersen, L. (1993) Particle mesh Ewald: an N · log(N) method for Ewald sums in large systems. *J. Chem. Phys.*, **98**, 10089–10092.
63. Berendsen, H.J.C., Postma, J.P.M., van Gunsteren, W.F., Di Nola, A. and Haak, J.R. (1984) Molecular dynamics with coupling to an external bath. *J. Chem. Phys.*, **81**, 3684–3690.
64. Gremer, L., Merbitz-Zahradnik, T., Dvorsky, R., Cirstea, I.C., Kratz, C.P., Zenker, M., Wittinghofer, A. and Ahmadian, M.R. (2011) Germline KRAS mutations cause aberrant biochemical and physical properties leading to developmental disorders. *Hum. Mutat.*, **32**, 33–43.
65. Hemsath, L. and Ahmadian, M.R. (2005) Fluorescence approaches for monitoring interactions of Rho GTPases with nucleotides, regulators, and effectors. *Methods*, **37**, 173–182.
66. Jaiswal, M., Dubey, B.N., Koessmeier, K.T., Gremer, L. and Ahmadian, M.R. (2012) Biochemical assays to characterise Rho GTPases. *Methods Mol. Biol.*, **827**, 37–58.
67. Eberth, A. and Ahmadian, M.R. (2009) In vitro GEF and GAP assays. *Curr. Protoc. Cell Biol.*, **43**, 14.9.1–14.9.25.
68. Cirstea, I.C., Gremer, L., Dvorsky, R., Zhang, S.C., Piekorz, R.P., Zenker, M. and Ahmadian, M.R. (2013) Diverging gain-of-function mechanisms of two novel KRAS mutations associated with Noonan and cardio-facio-cutaneous syndromes. *Hum. Mol. Genet.*, **22**, 262–270.
69. Sulston, J.E. and Hodgkin, J. (1988) Methods. In Wood, W.B. and The Community of *C. elegans* Researchers (ed.), *The Nematode Caenorhabditis Elegans*. Cold Spring Harbor Laboratory Press, Cold Spring Harbor, NY, pp. 587–606.
70. Mello, C.C., Kramer, J.M., Stinchcomb, D. and Ambros, V. (1991) Efficient gene transfer in *C. elegans*: extrachromosomal maintenance and integration of transforming sequences. *EMBO J.*, **10**, 3959–3970.

Journal of Human Genetics (2014) 59, 314–320

www.nature.com/jhg

ORIGINAL ARTICLE

Oculofaciocardiodental syndrome: novel *BCOR* mutations and expression in dental cells

Thunyaporn Surapornsawasd[1], Takuya Ogawa[1,2], Michiko Tsuji[1] and Keiji Moriyama[1,2]

Oculofaciocardiodental (OFCD) syndrome is a rare X-linked dominant condition. Mutations in *BCOR* have been described as causal in OFCD syndrome. Almost all *BCOR* mutations result in premature termination codons (PTCs); therefore, nonsense-mediated mRNA decay (NMD) might have an important role in pathogenesis. The purpose of this study was to identify *BCOR* mutations in two OFCD patients, if it present, and to clarify the pathogenesis of radiculomegaly using one OFCD patient's pulp and periodontal ligament (PDL) cells. In our genetic analysis, two novel *BCOR* mutations were found. We also examined the transcript levels and the effects of NMD using cultured pulp and PDL cells from one affected patient. *BCOR* expression was normal in pulp but reduced in PDL cells, which is consistent with the higher rates of NMD in PDL cells. The mutant PDL cells had unstable mutant transcripts and proliferated faster than did wild-type cells, but mutant pulp cells appeared normal by these measures. In summary, the nonsense and frameshift mutations, which introduce PTCs, were found to contribute to OFCD syndrome in our two patients. Furthermore, in PDL cells, the mutation resulting in a PTC corresponded to greater NMD, unstable mutant transcripts and increased cell proliferation, which may contribute to hyperactive root formation.
Journal of Human Genetics (2014) **59**, 314–320; doi:10.1038/jhg.2014.24; published online 3 April 2014

Keywords: nonsense-mediated mRNA decay; oculofaciocardiodental syndrome; radiculomegaly; X-linked dominant

INTRODUCTION

Oculofaciocardiodental (OFCD, MIM 300166) syndrome is a rare, X-linked dominant hereditary trait with skewed X inactivation[1] in heterozygous females. Males with this syndrome cannot survive because of embryonic lethality.[2–4] OFCD syndrome is characterized by microphthalmia, congenital cataracts, facial dysmorphic features, congenital heart defects and dental anomalies.[1,3–7] Most affected OFCD patients have remarkable dental anomalies, including radiculomegaly with prolonged dental roots and widely open apices, most often in the canine roots.[4,6–8] Recently, mutations in the *BCOR* gene, which encodes the BCL6 corepressor, have been found to cause OFCD syndrome.[3,5] The *BCOR* gene is located on the short (p) arm of the X chromosome at the position 11.4. *BCOR* is a transcriptional corepressor that was originally identified by its ability to interact with the site-specific transcriptional repressor BCL-6.[9]

Previous studies have reported that, owing to the phenotypic overlap, OFCD and Lenz microphthalmia syndrome are allelic disorders.[3,5,7] Lenz microphthalmia syndrome is an X-linked recessive condition comprising microphthalmia/anophthalmia with mental retardation, malformed ears, skeletal, renal and urogenital anomalies. Two genetic loci that can cause what is currently considered Lenz microphthalmia syndrome have been reported: one is located at Xq27-q28 (MCOPS1; MIM 309800),[10] and the second is located at Xp11.4 (MCOPS2; MIM 300166).[3,11] The MCOPS2 form of Lenz microphthalmia syndrome has been shown to be caused by mutations in the *BCOR* gene. A single missense change, c.254C>T (p.P85L), in *BCOR* has been found in patients of a family with MCOPS2.[3] However, *BCOR* mutations are not a major cause of X-linked microphthalmia in males.[5]

A previous study in mouse embryos showed that *Bcor* expression was observed in the eye, brain, neural tube and branchial arches and that the expression levels correlated with the tissues affected in OFCD patients.[12] *BCOR* has multiple roles in the complex process of human development, including the correction of lateral organization.[13] Moreover, *BCOR* maintains tissue homeostasis and gene silencing through epigenetic mechanisms.[2,12,14] *BCOR* expression has been detected in both the dental epithelium and mesenchyme during tooth development in early embryogenesis, and *BCOR* expressed in the mesenchyme has an important role in proper tooth formation.[15] Moreover, mutant *BCOR* increased the osteo-dentinogenic potential of mesenchymal stem cells (MSCs) by inducing AP-2$^{\alpha}$, and it increased the cell proliferation rate.[2] However, the mechanism of hyperactive root formation in OFCD syndrome is still unclear.

Almost all of the mutations identified in individuals with OFCD syndrome result in predicted premature termination codons (PTCs) and have similar phenotypic consequences.[3–5,7] A mutation that leads to PTC will be transcribed into mRNA and then translated into a truncated protein. The mRNA will be degraded by a protective

[1]Maxillofacial Orthognathics, Graduate School, Tokyo Medical and Dental University, Tokyo, Japan and [2]Hard Tissue Genome Research Center, Tokyo Medical and Dental University, Tokyo, Japan
Correspondence: Dr T Ogawa, Maxillofacial Orthognathics, Graduate School, Tokyo Medical and Dental University, 1-5-45, Yushima, Bunkyo-ku, Tokyo 113-8549, Japan.
E-mail t-ogawa.mort@tmd.ac.jp
Received 28 November 2013; revised 20 February 2014; accepted 28 February 2014; published online 3 April 2014

mechanism in the cell called nonsense-mediated mRNA decay (NMD) to shield cells from dominant-negative or deleterious gain-of-function activities of mutant proteins. The efficiency of NMD is an inherent characteristic and varies among different cells.[16,17] NMD may exert a beneficial, neutral or harmful effect, depending on the location of the PTC in the transcript and the properties of the truncated protein. NMD can also contribute to a disease phenotype when it inhibits the expression of partially functional proteins.[18] According to previous studies of *BCOR* mutations, it is likely that NMD prevents the truncated proteins from being expressed *in vivo*.[3,6] However, NMD was not confirmed because of the severely skewed X-inactivation in blood leukocytes.[3,13] Here, for the first time, we report alterations in the transcript levels of *BCOR* due to NMD in cultured pulp and periodontal ligament (PDL) cells from one affected patient.

In our study, we identified novel mutations in the *BCOR* genes of two affected OFCD patients. In addition, PDL and pulp tissue were harvested from a first premolar of one affected patient that was extracted for orthodontic purposes and then cultured. We performed an analysis of NMD, RNA stability and cell proliferation on these two cell types, which confirmed our hypothesis that the mutant RNAs were degraded by NMD mechanisms leading to haploinsufficiency of the *BCOR* protein, and compromised *BCOR*-mediated regulatory activities in root formation.

MATERIALS AND METHODS

Subjects

Two female OFCD patients (aged 27 years and 18 years) and three healthy subjects were patients of the Department of Orthodontics, Dental Hospital, Tokyo Medical and Dental University, Japan. The healthy patient 1's parents and the healthy patient 2's mother were also included in the genetic analysis. The clinical findings and orthodontic analysis of both OFCD patients at the first visit were previously described by Tsukawaki *et al*.[19] The diagnosis of OFCD syndrome was based on a distinct pattern of eye, craniofacial, heart and dental anomalies. Informed consent was obtained from both patients and their parents. The human subject research described here was approved by the Ethical Review Committee of the Tokyo Medical and Dental University.

Mutation analysis

Genomic DNA was extracted from buccal swabs with the QIAamp DNA Mini kits (Qiagen, Germantown, MD, USA) according to the manufacturer's protocol. Coding exons and flanking introns of the *BCOR* gene (15 exons: GenBank accession no. AY316592) were amplified by conventional PCR using KOD-Plus (TOYOBO, Lifescience, Tokyo, Japan). The primer sequences and PCR conditions used for the *BCOR* gene were previously described.[7] All novel mutations that we found were submitted to Leiden Open Variation Database (http://databases.lovd.nl/shared/genes/BCOR). The presence of a PCR product was verified by gel electrophoresis of the PCR product on a 1.5% agarose gel stained with ethidium bromide. Thereafter, the PCR products were directly sequenced with the BigDye Terminator v3.1 Cycle Sequencing Kit (Applied Biosystems, Life Technologies, Foster City, CA, USA) on a Perkin Elmer PE 9700 Thermal Cycler. The mutations were evaluated for their disease-causing potential based on sequence alterations by the 'Mutation Taster' (http://www.mutationtaster.org/)[20] and confirmed with the Japanese Single Nucleotide Polymorphisms Database (http://snp.ims.u-tokyo.ac.jp/index.html).

Cell culture

The first premolars of patient 2 and three healthy subjects were extracted for orthodontic reasons. The PDL surrounding the apical 1/3 of the root and apical pulp tissues were harvested using an aseptic technique, as previously described.[21–23] The cells were cultured in αMEM (Wako, Osaka, Japan) supplemented with 10% fetal bovine serum (Gibco, Life Technologies, Paisley, UK) and penicillin-streptomycin (Gibco). All cultures were maintained in a humidified, 5% CO_2 atmosphere at 37 °C. No cells were passaged more than five times (P5). Genomic DNA was extracted from both pulp and PDL cells to confirm the sequence of the *BCOR* gene.

RNA preparation

Total RNA was isolated from cultured pulp and PDL cells from the patient and three normal controls using ISOGEN (Nippon Gene, Toyama, Japan). Reverse transcription was performed using 1 μg of total RNA and the QuantiTect Reverse Transcription Kit (Qiagen) in a total volume of 20 μl according to the manufacturer's instructions.

Characterization of the cultured cells

Transcript levels of vimentin (*VIM*) and keratin 14 (*KRT14*) were measured and used as markers of mesenchymal and epithelial cells, respectively. Total RNA extraction, cDNA synthesis and conventional PCR were performed. The primers used were as follows: *VIM*, forward, 5′-AGGTGGACCAGCTAACC AAC-3′ and reverse, 5′-AGCATCTCCTCCTGCAATTT-3′; *KRT14*, forward, 5′-ATTGAGAGCCTGAAGGAGGA-3′ and reverse, 5′-ATTGACATCTCCACC CACCT-3′; and *β-ACTIN*, forward, 5′-CATGTACGTTGCTATCCAGGC-3′ and reverse, 5′-CTCCTTAATGTCACGCACGAT-3′. The PCR cycling conditions for *VIM*, *KRT14* and *β-ACTIN* consisted of an initial denaturation step at 94 °C for 3 min, 30 cycles of amplification (15 s at 94 °C; 10 s at 55 °C; 45 s at 72 °C) and a final extension step at 72 °C for 4 min. Gel electrophoresis was performed for the semi-quantitative evaluation of gene expression.

Real-time PCR

Each cDNA was used as a template for the quantitative analysis of *BCOR* mRNA expression with a 7300 Real-Time PCR system (Applied Biosystems). The real-time PCR reactions were performed using the Power SYBR Green PCR master mix (Applied Biosystems), according to the manufacturer's instructions. The total RNA input into each reaction was constant. The primers used were as follows: *BCOR*, forward, 5′-TCCTCGACTCGCCAAAT AAG-3′ and reverse, 5′-TGGCATAGTGCTTGTGGAAC-3′; *β-ACTIN*, forward, 5′-CATGTACGTTGCTATCCAGGC-3′ and reverse, 5′-CTCCTTAATGTCACG CACGAT-3′. The real-time PCR conditions are available on request.

Analysis of NMD

We examined the levels of mutant transcripts following treatment with cycloheximide (CHX), a general inhibitor of translation elongation. Because NMD is translation-dependent, CHX treatment leads indirectly to the inhibition of NMD.[16,24] Cells were grown in two 10-cm-diameter cell culture dishes until they reached 70% confluence. The medium was changed and replaced with 5 mg CHX (Wako) dissolved in 10 ml complete medium (for a final CHX concentration of 500 μg ml^{-1}) and then incubated at 37 °C. Total RNA was extracted from the cells at 0 and 6 h after adding CHX, and then *BCOR* expression was evaluated using real-time PCR. The experiments were performed in triplicate.

Analysis of mRNA stability

Cells grown in three 10-cm-diameter cell culture dishes were treated with 1 μg ml^{-1} of actinomycin D (Wako) and incubated at 37 °C. Total RNA was isolated from the cells at 0, 3 and 6 h after adding actinomycin D, and *BCOR* expression was evaluated using real-time PCR. The experiments were performed in triplicate.

Cell proliferation rate

To monitor cell proliferation, MTT assays were performed. Pulp and PDL cells from the patient and normal controls were plated in a 96-well plate with a volume of 100 μl per well (7500 total cells). Six wells were allotted per cell type, and wells with complete medium served as a negative control. All cells were incubated at 37 °C. Pulp cells were incubated for 1, 2, 3 or 4 days, and PDL cells were incubated for 24, 36 or 48 h. Subsequently, each well was incubated with 20 μl of 5 mg ml^{-1} MTT (Sigma, St Louis, MO, USA) at 37 °C for 3.5 h. The MTT solution was removed, and 150 μl MTT solvent (4 mM HCl, 0.1%